Theoretical Investigation of the Electrochemical Oxidation of H_2 and CO Fuels on a Ruddlesden-Popper $SrLaFeO_{4-\delta}$ Anode

Nicholas A. Szaro^a, Salai Cheettu Ammal^a, Fanglin Chen^b, Andreas Heyden^a*

^a Department of Chemical Engineering, University of South Carolina, 301 South Main Street, Columbia, South Carolina 29208, United States

^b Department of Mechanical Engineering, University of South Carolina, 300 South Main Street, Columbia, South Carolina 29208, United States

*Email: <u>heyden@cec.sc.edu</u>

Abstract

The electrochemical oxidation of H₂ and CO fuels have been investigated on the Ruddlesden-Popper layered perovskite, SrLaFeO_{4- δ} (SLF), under anodic solid oxide fuel cell conditions using periodic density functional theory and microkinetic modeling techniques. Two distinct FeO₂plane terminated surface models differing in terms of the underlying rocksalt layer (SrO or LaO) are used to identify the active site and limiting factors for the electro-oxidation of H₂, CO, and syngas fuels. Microkinetic modeling predicted an order of magnitude higher turnover frequency for the electro-oxidation of H₂ compared to CO for SLF at short circuit conditions. The surface model with an underlying SrO layer was found to be more active with respect to H₂ oxidation than the LaO-based surface model. At an operating voltage of less than 0.7 V, surface H₂O/CO₂ formation was found to be the key rate-limiting step and the surface H₂O/CO₂ desorption was the key charge transfer step. In contrast, the bulk oxygen migration process was found to affect the overall rate at high cell voltage conditions above 0.9 V. In the presence of syngas fuel, the overall electrochemical activity is derived mainly from H₂ electro-oxidation and CO₂ is chemically shifted to CO via the reverse water-gas shift reaction. Substitutional doping of a surface Fe atom with Co, Ni, and Mn revealed that the H₂ electro-oxidation activity of FeO₂plane terminated anodes with an underlying LaO rocksalt layer can be improved with dopant introduction, with Co yielding a three orders of magnitude higher activity relative to the undoped LaO surface model. Constrained ab initio thermodynamic analysis furthermore suggested that the SLF anodes are resistant towards sulfur poisoning both in the presence and absence of dopants. Our findings reflect the role of various elements in controlling the fuel oxidation activity of SLF anodes that could aid the development of new Ruddlesden-Popper phase materials for fuel cell applications.

Keywords: SrLaFeO₄; Ruddlesden-Popper oxide; H₂ oxidation; CO oxidation; Density functional theory; Microkinetic modelling, Solid Oxide Fuel Cell

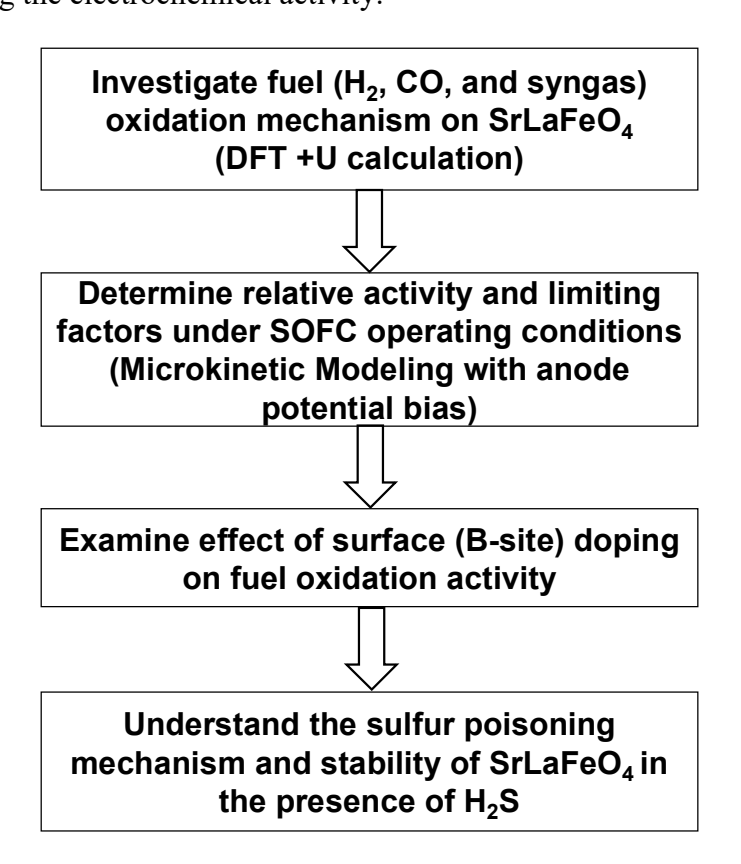
1. Introduction

Solid oxide fuel cells (SOFCs) are solid-state electrochemical devices that display the promising ability to oxidize both hydrogen gas and hydrocarbon-based fuels directly into electricity with high efficiency ^{1,2}. SOFC adoption for practical use is limited due to high operating temperatures and material decomposition resulting from mechanical and chemical instabilities³. Selection of stable and active anode materials is a crucial part of SOFC development since fuel oxidation occurs at the anode. Nickel-yttria stabilized zirconia (Ni/YSZ) is considered the state-of-the-art anode cermet material for SOFC applications; however, it suffers from redox instability, particle agglomeration, and sulfur poisoning ⁴. Extensive research has been performed to identify alternate anode materials that can circumvent these drawbacks of Ni/YSZ. A recent review summarizes the reports focusing on single-phase and composite electrode materials that are both sulfur resistant and ionically conductive at or below 800 °C 5. Perovskite-based mixed ionic and electronic conductors (MIECs) such as LSCM and SFMO have been proposed as promising alternative candidates for anodic applications ^{6–8}. In addition to the traditional perovskite-based compounds, the Ruddlesden-Popper (RP) phase materials with K_2NiF_4 -type $(A_{n+1}B_nO_{3n+1}, n=1 \text{ to } \infty)$ structure have also received attention as potential candidates for SOFC applications. Here, the A-site refers to an alkali, an alkaline earth, or a rare earth metal; and the B-site refers to a transition metal.

The layered RP oxides display high ionic conductivity and catalytic activity for the oxygen reduction reaction, and thus being developed for use in metal-air batteries, supercapacitors, and cathodic applications $^{9-13}$. Recent studies have also examined the performance of RP oxides as anodes for SOFCs. Xu et. al. demonstrated that SrLaFeO_{4- δ} (SLFO_{4- δ} or SLF) has chemical compatibility with the commonly used Sm_{0.2}Ce_{0.8}O_{1.9} (SDC) and

La_{0.8}Sr_{0.2}Ga_{0.85}Mg_{0.15}O₃ (LSGM) electrolytes and exhibits electro-catalytic activity towards wet H_2 (P_{max} of 0.63 W/cm² at 800 °C) with sulfur resistance for greater than 80 hours under $H_2 + 50$ ppm H₂S feed ¹⁴. To further enhance the catalytic activity of SLF, Wang et. al. synthesized a composite anode of exsolved Fe-Ni alloy nanoparticles on a SLF substrate that displayed increased catalytic activity relative to pure SLF, especially at temperatures lower than 700 °C ¹⁵. In another study, Wu et. al. reported that a composite anode of exsolved Fe-Ni alloy nanoparticles on a SrLaFe_{0.75}Ni_{0.25}O₄ substrate displayed a power output of 0.54 W/cm² at 800 °C under H₂ + 1000 ppm H₂S feed ¹⁶. In addition to Ni, other transition metals, such as Co and Mn – have also been utilized to modulate SLF performance. For example, Chang et. al. used SLF as a pure catalyst layer with exsolved Co-Fe alloy nanoparticles for a direct methane-based anode displaying coking resistance ¹⁷. Furthermore, Park et. al. utilized Co-Fe alloy nanoparticles on a related material, Sr_{0.8}La_{1.2}Co_{0.4}Fe_{0.6}O₄ for direct H₂ oxidation and observed max power density of 0.73 W/cm² 18 , Li et. al. used a Fe₃Co₂ + Sr_{0.8}La_{1.2}Mn_{0.4}Fe_{0.6}O₄ anode to display excellent activity under 200 ppm H₂-H₂S conditions ¹⁹, and Chung et. al. displayed a max power density of 0.72 W/cm 2 with Fe + Sr $_{0.8}$ La $_{1.2}$ Mn $_{0.4}$ Fe $_{0.6}$ O₄ in the presence of H $_2$ 20 . Overall, these experimental studies demonstrate that SLF (with its B-site doped conformers) can be regarded as a promising anode material class due to its observed native electrochemical activity, stability under concentrated sulfur feeds, and ability to serve as an exsolved nanoparticle substrate. However, a deeper understanding of the fuel oxidation mechanism on these substrates is lacking and the role of B-site dopant metals in the electrochemical activity and sulfur resistance is not well understood, which are crucial for the development of alternative RP oxide-based anode materials.

Computational studies performed over RP oxides have focused on understanding the oxygen reduction process over Sr₃Fe₂O₇ ²¹ and La₂NiO₄ ^{22,23} materials for cathodic applications. While the theoretical studies on anode reactions over RP oxides are rare, the fuel oxidation mechanism has been widely investigated over perovskite materials for anode applications. Suthirakun et. al. and Han et. al. investigated H₂ oxidation mechanism on the double perovskite Sr₂Fe_{1.5}Mo_{0.5}O₆ (SFMO) ^{24,25} and Ren et. al. studied CO₂ reduction on the (Sr,La)(Fe,Mn,Ni)O₃ perovskite for electrolysis applications ²⁶. Heyden and coworkers examined the oxidation mechanism of CO and syngas over SFMO ²⁷ and further explored different poisoning mechanisms of sulfur via thermodynamic analysis on SFMO ²⁸. These studies provided a fundamental understanding of reactions at the anode and the role of different elements in enhancing/inhibiting the electrochemical activity.



Scheme 1: Outline of the fuel oxidation study on the SrLaFeO_{4-δ} anode

Herein, we conducted a mechanistic investigation of H₂, CO, and syngas fuel oxidation reactions on SrLaFeO_{4-δ} using a combination of density functional theory (DFT) and microkinetic modeling techniques as illustrated in Scheme 1. We examined the electrochemical activity of different SLF surfaces with respect to cell voltage and explored the sulfur poisoning mechanism on these surfaces. Furthermore, we analyzed the effects of a single-atom surface B-site doping with Co, Mn, and Ni dopants on the kinetic activity of H₂ oxidation and sulfur stability. We used standard SOFC operating conditions to determine rate-controlling steps and polarization curves that could aid the design of future RP-based materials for SOFC applications.

2. Methods

Electronic energies are obtained with spin-polarized Kohn-Sham DFT+U calculations with periodic boundary conditions using the Vienna Ab Initio Simulation Package (VASP) version 5.4.4 ^{29,30}. Electron exchange-correlation effects were evaluated by utilizing the generalized gradient approximation (GGA) with the Perdew, Burke, and Ernzerhof (PBE) functional ^{31,32}. Dudarev's approach for DFT+U calculations is used to correct the inadequate description of localized 3d electrons on transition metals ³³. The U-J parameter of 4.0 was used for Fe d-block electrons in accordance with earlier reports ^{34,35}. In the case of dopants, the U-J parameters of 3.32 (Co), 3.9 (Mn), and 6.0 (Ni) eV were chosen based on the values utilized by the Materials Project ^{36,37}. The nuclei and core electrons were represented by the frozen-core projector-augmented wave (PAW) approach using the following valence configurations: Sr (4s2 4p6 5s2), La (5s2 5p6 5d1 6s2), Fe (3p6 3d6 4s2), Co (3p6 4s2 3d7), Mn (3p6 4s2 3d5), Ni (3s2 3p6 4s2 3d8), O (2s2 2p4), H (1s), and C (2s2 2p2) ³⁸. The plane-wave basis set was set to a kinetic cutoff of 700 eV. Integration over the Brillouin zone used the Gaussian method with a

smearing width of 0.05 eV for all calculations. The convergence criteria for electronic energy and ionic relaxations were set to 10^{-6} eV and 0.05 eV/Å, respectively. Ferromagnetic (FM) ordering is chosen as the initial magnetic moment configuration for all transition metals. While the single bulk unit cell calculations utilized a $9 \times 9 \times 5$ Monkhorst-Pack (MP) k-point mesh 39 , the bulk vacancy calculations were carried out with a $2 \times 2 \times 1$ bulk structure supercell utilizing a $5 \times 5 \times 3$ MP k-point mesh as adopted in our earlier work on $(Sr_{1-x}Pr_x)_2FeO_{4\pm\delta}$ RP oxide 35 . Fuel oxidation mechanisms were examined on $3 \times 3 \times 1$ surface slab models $(1.5 \times 1.5 \times 1$ supercell units) using a $3 \times 3 \times 1$ MP k-point mesh. Dipole and quadrupole corrections to the energy were incorporated using a modified version of the Markov and Payne method 40 . For transition state (TS) structure calculations, we used the VTST implementation of the climbing image nudged elastic band (CI-NEB) and dimer methods $^{41-44}$. All spring forces are converged to 0.05 eV/Å. The VESTA 3 program is used to visualize the optimized structures 45 .

The following expression was utilized to calculate the chemical potential (μ_i) of any gaseous species (H₂, O₂, CO, H₂O, CO₂, H₂S, and CH₄),

$$\mu_i = \mu_i(T, p^\circ) + k_B T \ln \left(\frac{p_i}{p^\circ}\right) \tag{1}$$

where $\mu_i(T, p^\circ)$ is calculated from the partition functions of the gaseous species referenced to a pressure (p°) of 1 atm, k_B is the Boltzmann constant, T is temperature, and p_i is the applied partial pressure of a gaseous species. Details regarding the calculation of these free energies are described in Section S1 of the Supporting Information. Since GGA tends to overestimate the binding energy of O_2 , the energy of O_2 molecule (E_{O2}) is calculated using the following correction scheme based on the H_2O splitting reaction $^{46-48}$:

$$E_{O2} = 2[(E_{DFT,H2O} + E_{ZPE,Exp.\ H2O}) - (E_{DFT,H2} + E_{ZPE,Exp.\ H2}) - E_{Exp.\ HOF}] - E_{ZPE,Exp.\ O2}$$
(2)

Here, $E_{DFT,i}$ is the energy of the corresponding gas molecule calculated with the PBE functional, $E_{ZPE,Exp,i}$ is the experimental zero-point energy, and $E_{Exp.\ HOF}$ is the experimental heat of formation of a gas-phase H₂O molecule. In addition, PBE is known to underestimate the gas phase energy of the CO molecule ⁴⁹; and therefore, we utilized a correction of -0.42 eV as determined by Ammal and Heyden ²⁷. Adsorption free energies of all intermediates, $G_{ads,i}$, were calculated based on the following equations ⁵⁰:

$$G_{ads,i} = G_{slab+intermedia} ,_{i} - G_{slab} - N_{H}\mu_{H} - N_{O}\mu_{O} - N_{C}\mu_{C}$$

$$(3)$$

$$\mu_H = \frac{1}{2}\mu_{H2} \tag{4}$$

$$\mu_0 = \mu_{H20} - \mu_{H2} \tag{5}$$

$$\mu_C = \mu_{CH4} - 2\mu_{H2} \tag{6}$$

 $G_{slab+intermediate,i}$ is the free energy of the surface with adsorbed intermediate, G_{slab} is the free energy of the bare surface model, and the chemical potentials of the molecules, μ_{H2} , μ_{O2} , and μ_{CH4} are calculated using eqn. 1. N_H , N_O , and N_C are the number of H, O, and C atoms in the adsorbed surface intermediates. The reaction (ΔG_i^{rxn}) and activation (ΔG_i^{\dagger}) free energies of an elementary step were calculated using the following equations:

$$\Delta G_i^{rxn} = \sum_j \nu_{ij} G_{ads,j}^i \tag{7}$$

$$\Delta G_i^{\ddagger} = G_{ads,i}^{\ddagger} - \sum G_{ads,i}^R \tag{8}$$

 v_{ij} and $G^i_{ads,j}$ are the stoichiometric coefficient and adsorption energy of an intermediate j in reaction step i, respectively. We note here that all reaction and activation free energies are independent of the reference state.

For an adsorption elementary reaction, $A + * \to A^*$, where * and A^* represent an empty site and adsorbed species on the slab model, respectively, collision theory was used to calculate the forward or adsorption rate constant $(k_{for,i})$.

$$k_{for,i} = \frac{10^5 S_{unit}}{(2\pi m_i k_B T)^{\frac{1}{2}}} (s^{-1} atm^{-1})$$
 (9)

Here, m_i is the molecular weight of the adsorbing species and S_{unit} is the surface area of our slab models (1.39 × 10⁻¹⁸ m²). A sticking coefficient of unity is used in all simulations ^{24,25}. Transition state theory was used to calculate the forward rate constant (k_{for}) for a surface reaction $A^* \to B^*$.

$$k_{for} = \frac{k_B T}{h} e^{\frac{-\Delta G_i^{\ddagger}}{k_B T}} \tag{10}$$

The equilibrium constant (K_{eq}) for an elementary reaction is computed with the following equation:

$$K_{eq} = e^{\frac{-\Delta G_i^{rxn}}{k_B T}} \tag{11}$$

Based on the calculated forward and equilibrium constants for each elementary step, we constructed a microkinetic model as a set of ordinary differential equations. The microkinetic model is solved via MATLAB with ODE15s 51 . The steady-state solution provides a probability density for the system to occupy each discrete state and we refer to these probabilities as surface coverages or θ_i . The turnover frequency (TOF) of each pathway was calculated using the calculated surface coverages. For syngas fuel, we combined all elementary reactions from the H_2 and CO oxidation pathways into one microkinetic model. We used Campbell's degree of rate control ($X_{RC,i}$) to identify rate-controlling steps using the following expression 52,53 :

$$X_{RC,i} = \left(\frac{\partial \ln (TOF)}{\partial \ln (k_i)}\right)_{K_i, k_{j \neq i}}$$
(12)

The apparent activation energy (E_{app}) was calculated over a temperature range of 973 to 1373 K using the expression:

$$E_{app} = RT^2 \left(\frac{\partial \ln(TOF)}{\partial T} \right)_{P,v_i}$$
 (13)

3. Results and Discussion

3.1 Development of SLF Bulk and Surface Models

The bulk structure of SLF was optimized using the computational setup described above starting from the structure obtained from materials project entry mp-1218154 36,54,55 with a unit cell of 14 atoms and a space group of I4mm. The calculated lattice parameters (a = b = 3.929 (Å) and c = 12.626 (Å)) of this RP oxide are close to the experimental lattice parameters (a = b = 3.8750 (Å) and c = 12.727 (Å)) reported in the literature 14,56 . We utilized a 2 × 2 × 1 supercell (56 atoms) to compute the free energy of oxygen vacancy formation and the bulk vacancy-mediated migration energy as displayed in Figure 1(a). Details regarding the mechanics of the bulk vacancy-mediated migration are outlined in the Supporting Information Section S2. We calculated the free energy barrier of vacancy-mediated diffusion as 1.30 eV at T = 1073 K and $P_{02} = 10^{-20}$ atm 57 . This value is consistent with other n = 1 RP oxides with a 50% A-site doping ratio such as SrPrFeO₄ (1.3 eV) 35 and LaSrCoO₄ (~ 1.1 eV) 58 , respectively.

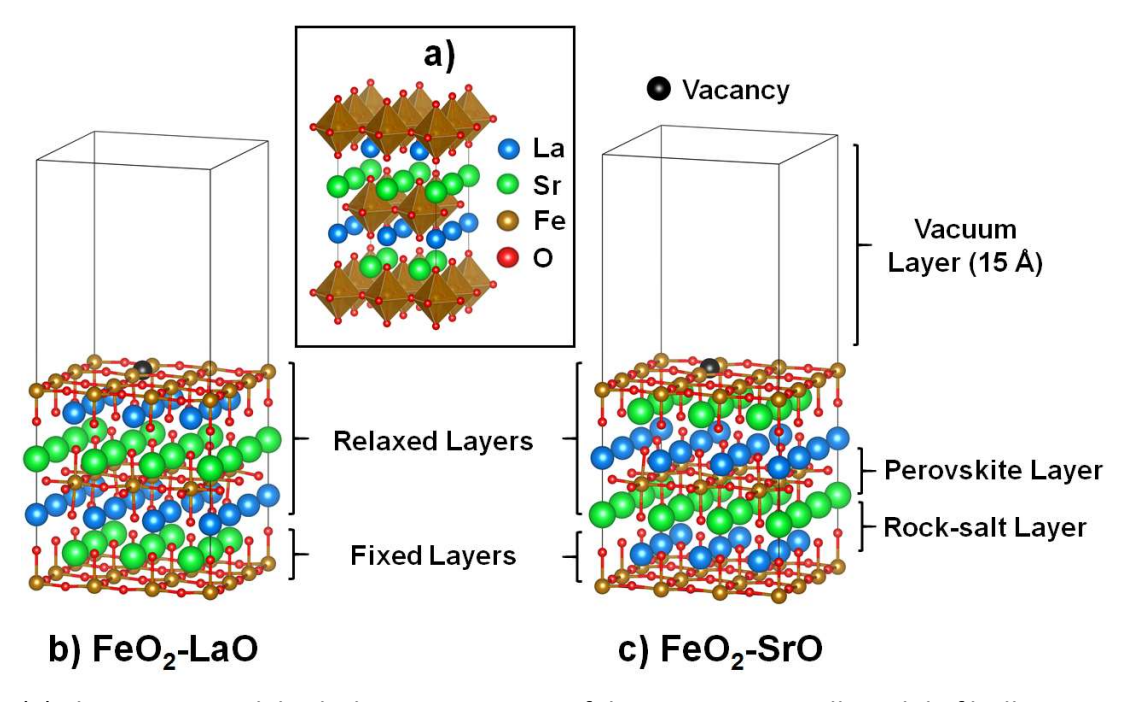


Figure 1: (a) The $2 \times 2 \times 1$ polyhedral representation of the I4mm supercell model of bulk SrLaFeO₄ (SLF) and (b-c) the $3 \times 3 \times 1$ unit cells of SLF (001) surface models where (b) FeO₂-LaO and (c) FeO₂-SrO represent the FeO₂-terminated surfaces with LaO or SrO in the second layer, respectively.

Computational studies performed over $Sr_{n+1}Fe_nO_{3n+1}$ RP oxides suggested that the (001) facet of these oxides is thermodynamically stable ⁵⁹ and kinetically active for O_2 reduction ²¹ and NO oxidation ⁶⁰. Therefore, the (001) surface models of SLF were constructed for the present study. Four possible (001) terminations are possible for SLF with two FeO₂-plane terminations and two rocksalt layer (LaO and SrO) terminations. Only the FeO₂-plane terminations are considered here because they are expected to be more catalytically active due to the ability of Fe to readily adopt different oxidation states relative to alkaline earth Sr or lanthanide La. The two FeO₂-terminated surfaces differ in terms of the nearest underlying rocksalt layer (LaO or SrO) as shown in Figure 1(b-c) and are designated as FeO₂-LaO and FeO₂-SrO surfaces. The SLF surface models were developed following the approach outlined by Akbay et. al. for the La₂NiO₄ RP oxide using a 2 × 2 × 4/3 unit cell model ²³. Here, we used a 3 × 3 × 1 unit cell slab model (1.5 × 1.5 × 1 supercell units) that was found to be large enough to avoid the interaction between

an adsorbent with its periodic replica and be computationally affordable. These slab models are composed of seven atomic layers and have a computed surface area of 1.39 × 10 ⁻¹⁸ m². A vacuum gap of 15 Å was used to minimize the interaction between images along the z-axis. The bottom-most FeO₂-plane and a rocksalt layer (e.g., 2 bottom layers) were fixed in all calculations to mimic a semi-infinite bulk crystal.

Oxygen nonstoichiometry via oxygen vacancies is expected for these RP oxides under low oxygen partial pressures (reducing conditions) found in SOFC anodic operating conditions. To capture a representative example of the SLF surface structure under SOFC operating conditions, we computed the Gibb's free energy of oxygen vacancy formation on each surface model that can determine the thermodynamic drive to form surface vacancies. We compute the free energy of surface vacancy formation as -0.83 and -2.56 eV for FeO₂-LaO and FeO₂-SrO, respectively, at anodic operating conditions (1073 K, $P_{O2} = 10^{-20}$ atm). As both surfaces indicate favorability to form oxygen vacancies on the FeO₂-plane, we utilized a representative model of a single surface oxygen vacancy for both surfaces, a model similar to the ones adopted by Akbay et. al., Zhou et. al., and Gu and Nikolla ^{22,23,61} for examining reactions on RP oxides. An expanded analysis of the oxygen vacancy density as a function of oxygen chemical potential is provided in Section S3 of the Supporting Information.

3.2 H₂ Oxidation Mechanism on SLF (001) Surfaces

The overall electrochemical oxidation of H₂ on the SLF anodes can be expressed (in Kröger-Vink notation ⁶²) as:

$$H_2(g) + O_0^{\times}(SLF) \to H_2O(g) + V_0^{\circ}(SLF) + 2e'$$
 (14)

Here, O_0^{\times} and V_0^{\cdots} refer to an oxygen atom and a doubly positive charged oxygen vacancy on the SLF surface, respectively. Based on the gas phase reaction free energy of $H_2 + \frac{1}{2} O_2 \rightarrow H_2O$ ($\Delta G = -2.2 \text{ eV}$; T = 1073 K, $P_{H2}^{anode} = 1 \text{ atm}$, $P_{O2}^{cathode} = 0.21 \text{ atm}$) the 2e' oxidation process should yield a cell voltage of 1.1 V. Figure 2 illustrates our proposed catalytic cycle for the oxidation of H_2 on the SLF (001) surface models with elementary reactions $R_{H2}1$ to $R_{H2}5$ occurring at an active site $*_{Fe} - O$, where $*_{Fe}$ represents an adsorbate free Fe atom on the surface.

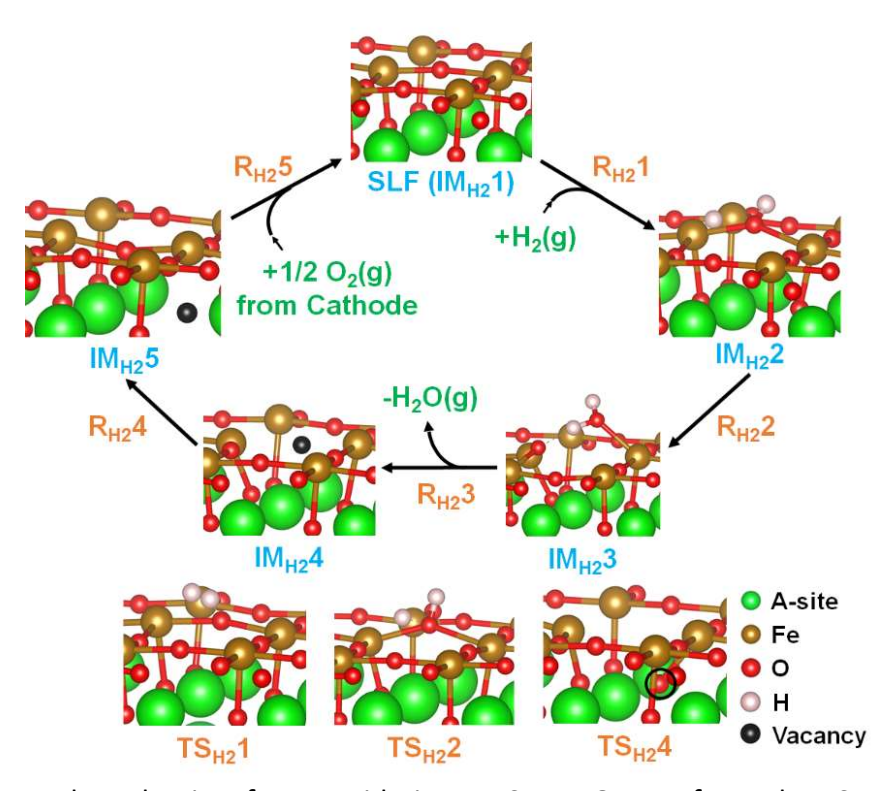


Figure 2: Proposed mechanism for H_2 oxidation on SrLaFeO_{4- δ} surface. The TS structures are in reference to the specific elementary reaction step. The vacancy (black) refers to the oxygen vacancy generated during H_2 oxidation.

All DFT+U calculations were performed on charge-neutral surface models; and therefore, the net charge on the elementary reactions $R_{H2}1$ to $R_{H2}5$ is zero. However, the electrochemical charge transfer process is considered in the microkinetic model. The first elementary step in the H_2 oxidation process ($R_{H2}1$) outlines the dissociative adsorption of the feed gas on a metal (Fe) site and a neighboring oxygen atom, forming a surface hydroxyl complex. The second ($R_{H2}2$)

and third (R_{H2} 3) elementary reactions describe the formation of H_2O on the surface and desorption of H_2O leading to the formation of surface oxygen vacancy ($V_0(S)$), respectively.

$$*_{Fe} - O(IM1) + H_2(g) \rightarrow H_{Fe} - OH(IM2)$$
 (R_{H2}1)

$$H_{Fe} - OH(IM2) \rightarrow *_{Fe} - OH_2(IM3)$$
 (R_{H2}2)

$$*_{Fe} - OH_2(IM3) \rightarrow H_2O(g) + *_{Fe} - V_O(S) (IM4)$$
 (R_{H2}3)

$$*_{Fe} - V_O(S) \text{ (IM4)} \rightarrow *_{Fe} - O - V_O(B) \text{ (IM5)}$$
 (R_{H2}4)

$$*_{Fe} - O - V_0(B) + \frac{1}{2}O_2 (cathode) \rightarrow *_{Fe} - O(IM1)$$
 (R_{H2}5)

The fourth elementary step $(R_{H2}4)$ outlines the migration of a bulk oxygen atom to the surface vacancy creating a bulk oxygen vacancy $(V_O(B))$ which is filled by an oxygen ion from the cathode in the final elementary step $(R_{H2}5)$. The replenishment of bulk oxygen vacancy at the anode by an oxygen ion from cathode $(R_{H2}5)$ involves multiple elementary processes such as, oxygen reduction reaction at the cathode $(V_{O,catho}^{""}) + \frac{1}{2}O_2(g) + 2e' \rightarrow O_{O,cathode}^{""})$, exchange of oxygen ion from the cathode to the electrolyte $(V_{O,electrolyte}^{""}) + O_{O,cathode}^{""})$, and final exchange of an oxygen ion from the electrolyte to the anode $(V_{O,anode}^{""}) + O_{O,electrolyte}^{""}) + O_{O,electrolyte}^{""})$, and final exchange of an oxygen ion from the electrolyte to the anode $(V_{O,anode}^{""}) + O_{O,electrolyte}^{""}) + O_{O,electrolyte}^{""}) + O_{O,electrolyte}^{""})$. We hold that the anode is primarily controlling SOFC performance since experimental studies observed that the introduction of Fe-Ni alloy particles to SLF anode improved the overall cell performance $(V_{O,anode}^{""})$. Therefore, we assumed that the oxygen reduction at the cathode and ion migration through the electrolyte are fast and considered the bulk vacancy-mediated migration of SLF oxygen to be the limiting factor for $R_{H2}5$. The SLF bulk oxygen diffusion barrier of 1.30 eV obtained from the bulk SLF DFT calculations is used to calculate the rate of $R_{H2}5$.

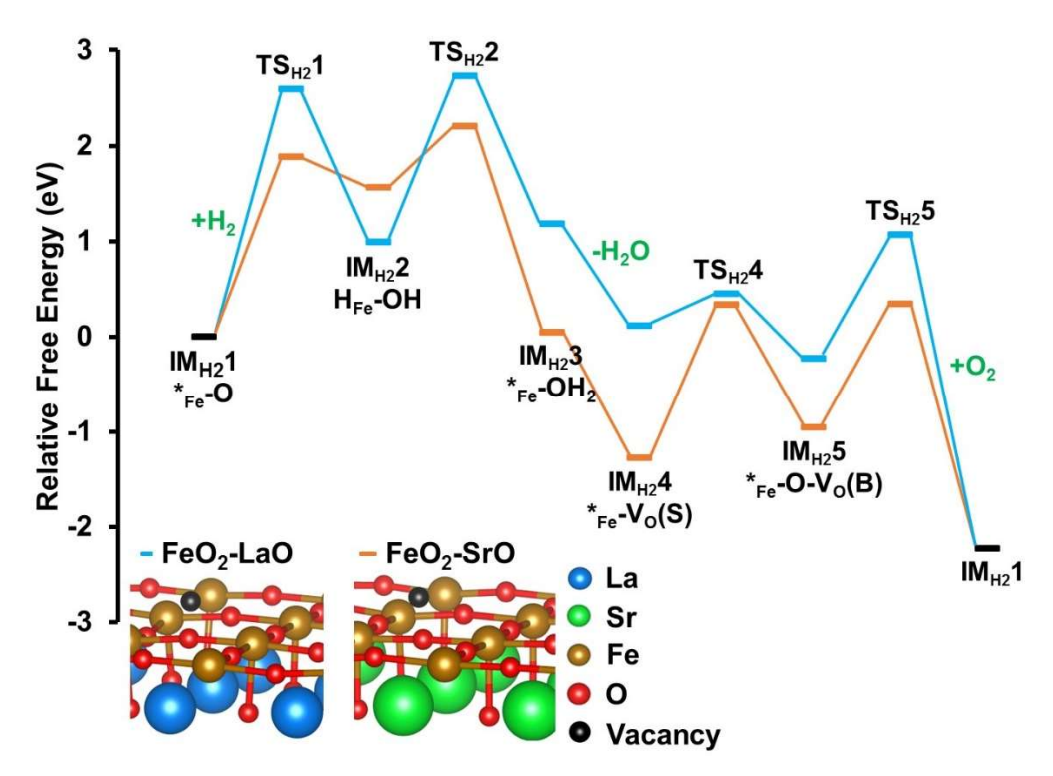


Figure 3: Relative free energy profiles (eV) for the H_2 oxidation network on the FeO₂-LaO (blue) and FeO₂-SrO (orange) surface models (T = 1073 K; P_{H2} (gas) = 1.0 atm; P_{H2O} (gas) = 0.03 atm; P_{O2} (gas) = 0.21 atm). All energies are with reference to the sum of the energies of the initial state (IM_{H2}1) and the gas phase molecules.

Figure 3 displays the free energy profiles for H_2 oxidation on the two FeO₂-terminated surfaces calculated at SOFC operating conditions. The transition state (TS) structures are numbered with reference to the corresponding elementary reaction steps. We note here that the initial active site ($IM_{H2}1$) of both FeO₂-LaO and FeO₂-SrO surface models already possess a surface oxygen vacancy. Thus, dissociative adsorption of H_2 ($R_{H2}1$) preferably occurs on the FeO site neighboring the surface vacancy forming H_{Fe} -OH ($IM_{H2}2$) where the H bonded to the Fe atom sits at the vacancy site (Figure 2). This process is endergonic by 1.00 eV on the FeO₂-LaO surface and 1.57 eV on the FeO₂-SrO surface. However, the process is kinetically favored over FeO₂-SrO ($\Delta G^{TS1} = 1.89$ eV) by 0.71 eV compared to FeO₂-LaO ($\Delta G^{TS1} = 2.60$ eV). The H_2O formation process which involves the transfer of an H atom from Fe to the hydroxyl group ($R_{H2}2$) is both kinetically and thermodynamically favored on the FeO₂-SrO ($\Delta G^{TS2} = 2.21$ eV;

 $\Delta G^{IM3} = 0.05 \text{ eV}$) relative to the FeO₂-LaO surface ($\Delta G^{TS2} = 2.73 \text{ eV}$; $\Delta G^{IM3} = 1.18 \text{ eV}$). The H_2O molecule in *Fe-OH2 (IM_{H2} 3) is weakly bound to the Fe atom with Fe-O distances of 2.11 Å and 2.30 Å on the FeO₂-LaO and FeO₂-SrO surfaces, respectively. While desorption of H₂O $(R_{H2}3)$ leading to the formation of surface oxygen vacancy $(IM_{H2}4)$ was found to be exergonic on both surfaces, the vacancy structure on the FeO₂-SrO surface is more stable by 1.39 eV compared to FeO₂-LaO surface. Furthermore, these results suggest that the formation of a second oxygen vacancy is favorable on the FeO₂-SrO surface under SOFC operating conditions, whereas it is slightly endergonic by 0.12 eV on the FeO₂-LaO surface. Migration of an oxygen from the subsurface layer to the surface oxygen vacancy $(R_{H2}4)$ generating a bulk oxygen vacancy $(IM_{H2}5)$ is an exergonic process by -0.34 eV for the FeO₂-LaO surface with a kinetic barrier of only 0.35 eV, whereas it is an endergonic process by 0.32 eV for the FeO₂-SrO surface and requires a kinetic barrier as high as 1.61 eV. A similar trend was observed by Gu and Nikolla 61 and in our earlier work on $(Sr,A^{3+})_{n+1}Fe_nO_{3n+1}$ -based RP oxides which revealed that the ease of formation and migration of bulk oxygen vacancy in the rocksalt layer of RP oxides depends on the oxidation state of the neighboring ion ³⁵. We complete the catalytic cycle by filling this bulk oxygen vacancy using an oxide ion from the cathode ($R_{H2}5$). Overall, the free energy profiles suggest that the H₂ oxidation process could be favorable on the FeO₂-SrO surface compared to the FeO₂-LaO surface. The TS corresponding to the water formation process $(TS_{H2}2)$ was found to be the highest energy state on the free energy profiles and could be rate-limiting for both the surfaces.

3.3 CO Oxidation Mechanism on SLF (001) Surfaces

The overall electrochemical oxidation of CO on the SLF anodes can be expressed as:

$$CO(g) + O_0^{\times}(SLF) \to CO_2(g) + V_0^{\circ}(SLF) + 2e'$$
 (15)

Here again, the gas phase reaction free energy of CO + $\frac{1}{2}$ O₂ \rightarrow CO₂ is calculated to be -2.2 eV at SOFC operating conditions and thus the maximum open-circuit voltage at these conditions for the 2e' oxidation process is 1.1 V. Figure 4 illustrates our proposed catalytic cycle for the oxidation of CO at an active site $*_{Fe}-0$ on the SLF (001) surface models which includes five elementary reactions defined as $R_{CO}1$ to $R_{CO}5$.

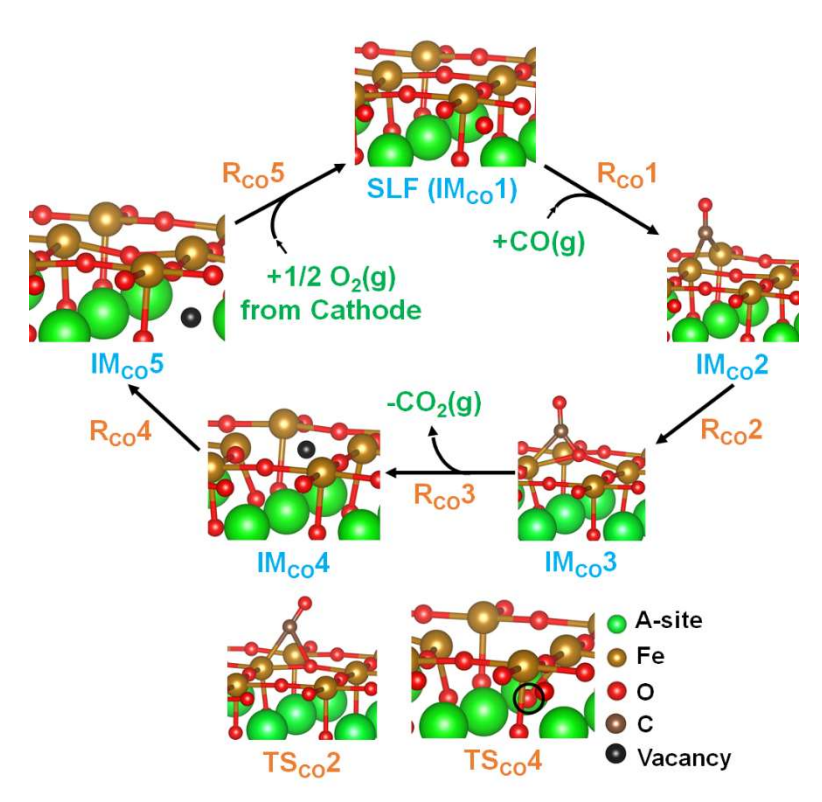


Figure 4: Proposed mechanism for CO oxidation on SrLaFeO_{4- δ} surface. The TS structures are in reference to the specific elementary reaction step. The vacancy (black) refers to the vacancy generated during CO oxidation.

The oxidation of CO on the SLF surface forming CO₂ and a surface oxygen vacancy can be described in the first 3 elementary reactions which involve adsorption of CO on the Fe metal site $(R_{CO}1)$, migration of CO to the neighboring oxygen forming CO₂ $(R_{CO}2)$, and desorption of CO₂ leaving a surface vacancy $(R_{CO}3)$.

$$*_{Fe} - O(IM1) + CO(g) \to CO_{Fe} - O(IM2)$$
 (R_{CO}1)

$$CO_{Fe} - O(IM2) \rightarrow *_{Fe} - OCO(IM3)$$
 (R_{CO}2)

$$*_{Fe} - OCO(IM3) \to CO_2(g) + *_{Fe} - V_0(S)(IM4)$$
 (R_{CO}3)

The surface vacancy structure $*_{Fe} - V_O(S)$ (IM4) formed after CO₂ desorption is the same vacancy structure obtained in the H₂ oxidation process and thus the last two steps R_{CO}4 – R_{CO}5 are equivalent to the elementary reactions R_{H2}4 – R_{H2}5.

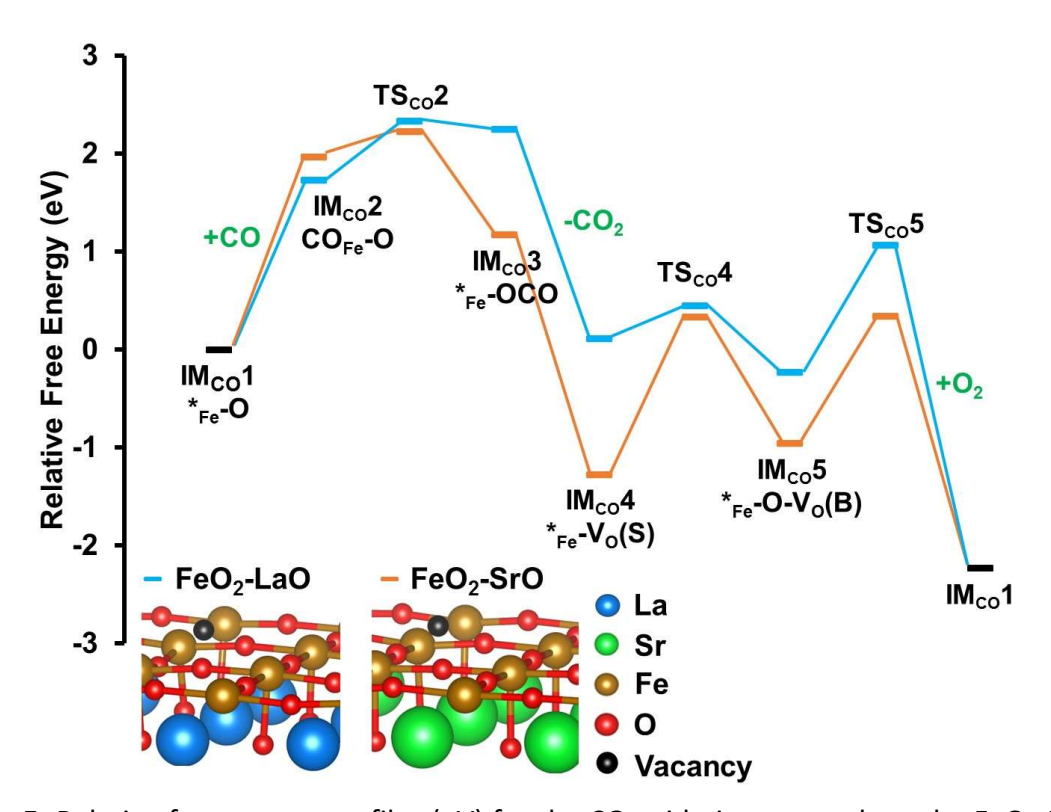


Figure 5: Relative free energy profiles (eV) for the CO oxidation network on the FeO₂-LaO (blue) and FeO₂-SrO (orange) surface models (T = 1073 K; P_{CO} (gas) = 1.0 atm; P_{CO2} (gas) = 0.03 atm; P_{O2} (gas) = 0.21 atm). All energies are with reference to the sum of the energies of the initial state (IM_{CO}1) and the gas phase molecules.

Figure 5 displays the free energy profiles calculated for the CO oxidation process on the two FeO₂-terminated surfaces at SOFC operating conditions. CO interacts weakly with the two Fe atoms next to the native surface oxygen vacancy site (R_{CO} 1) with average Fe-C bond distances of 2.32 and 2.27 Å on the FeO₂-LaO and FeO₂-SrO surfaces, respectively. The adsorption process is endergonic on both surfaces with Δ G ranging from 1.73 eV (FeO₂-LaO) to

1.97 eV (FeO₂-SrO). As observed in the case of H₂ oxidation process (Figure 3), the CO₂ formation (R_{CO} 2) and desorption (R_{CO} 3) processes are also thermodynamically more favorable on FeO₂-SrO surface compared to the FeO₂-LaO surface. The activation free energy of CO₂ formation (TS_{CO} 2) is 0.10 eV lower for the FeO₂-SrO surface relative to the FeO₂-LaO surface. Considering that TS_{CO} 2 is the highest energy state on the free energy profile for both surfaces, these results suggest that the FeO₂-SrO surface could be more active for CO oxidation compared to the FeO₂-LaO surface.

3.4 Insights from Microkinetic Modeling and Anode Bias Potential

Table 1: Forward rate (k_{for}) and equilibrium constants (K_{eq}) for all short-circuit reaction steps for H_2 and CO oxidation on the FeO_2 -LaO and FeO_2 -SrO surface models at 1073 K ($P_{H2,CO} = 1.00$ atm, $P_{H2O,CO2} = 0.03$ atm, and $P_{O2} = 0.21$ atm).

	FeO ₂ -LaC) Surface	FeO ₂ -SrO) Surface
H ₂ Oxidation	k _{for} (s ⁻¹)	K _{eq}	k _{for} (s ⁻¹)	K _{eq}
R _{H2} 1	1.40×10^{1}	2.09 × 10 ⁻⁵	1.84×10^{5}	2.64 × 10 ⁻⁷
R _{H2} 2	1.55×10^{5}	1.33×10^{-1}	2.13×10^{10}	1.30×10^{7}
R _{H2} 3	8.28×10^{12}	3.14×10^{3}	1.28×10^{14}	4.84×10^4
R _{H2} 4	5.79×10^{11}	3.99×10^{1}	6.43×10^{5}	3.14×10^{-2}
R _{H2} 5	1.76×10^{7}	5.39×10^9	1.76×10^{7}	3.59 × 10 ⁵
CO Oxidation	k _{for} (s ⁻¹)	K _{eq}	k _{for} (s ⁻¹)	K _{eq}
R _{CO} 1	2.11 × 10 ⁹	7.74 × 10 ⁻⁹	2.11 × 10 ⁹	5.73 × 10 ⁻
R _{CO} 2	3.25×10^{10}	3.63×10^{-3}	1.32× 10 ¹²	5.49×10^{3}
R _{co} 3	5.45×10^{17}	3.24×10^{8}	1.56×10^{19}	9.28 × 10 ⁹
R _{CO} 4	5.79×10^{11}	3.99×10^{1}	6.43×10^{5}	3.14 × 10 ⁻²
R _{CO} 5	1.76×10^{7}	5.39×10^9	1.76×10^{7}	2.13 × 10 ⁶

The forward rate and equilibrium constants of each elementary step of H₂ and CO oxidation reactions calculated from the DFT+U reaction energies and activation barriers for the FeO₂-LaO and FeO₂-SrO surfaces are summarized in Table 1. These data are used to build a microkinetic model to obtain further information on the relative rates, apparent activation barriers, and rate controlling factors for these surfaces. Since the fuel oxidation occurring in SOFCs also involves charge transfer processes, we adapted two types of microkinetic models that correspond to short circuit conditions and anode biasing. While the short circuit condition is equivalent to a thermochemical process, the anode biasing incorporates charge transfer effects. The results obtained from microkinetic analysis at short circuit conditions are summarized in Table 2. In accordance with the free energy profiles, the microkinetic analysis also revealed a three orders of magnitude higher turnover-frequency (TOF) and a 0.61 eV lower apparent activation energy for H₂ oxidation over FeO₂-SrO relative to the FeO₂-LaO surface. Campbell's degree of rate control analysis furthermore suggested that the H₂O formation process $(R_{H2}2, DRC = 0.92)$ is mainly rate-controlling for the FeO₂-SrO surface, whereas H₂ dissociation $(R_{H2}1, DRC = 0.22)$ also controls the overall rate to a small extent in the case of FeO₂-LaO surface. Nonetheless, surface water formation $(R_{H2}2)$ appears to be the key step to improve the performance of SLF-based anodes under thermochemical conditions. The higher TOFs and lower apparent activation energy predicted for the FeO₂-SrO surface indicates that this surface controls H₂ oxidation activity at all temperatures considered here under short circuit conditions.

Table 2: Degree of rate control (DRC), apparent activation energies (calculated in the temperature range of 973-1273 K), and turnover frequencies calculated for H_2 and CO oxidation over FeO_2 -LaO and FeO_2 -SrO surfaces at short circuit conditions (T = 1073 K, $P_{H2,CO}$ = 1.00 atm, $P_{H2O,CO2}$ = 0.03 atm, and P_{O2} = 0.21 atm).

H ₂ Oxidation		CO Oxidation	
FeO ₂ -LaO	FeO ₂ -SrO	FeO ₂ -LaO	FeO ₂ -SrO

				-		
Degree of Rate Control	R _{H2} 1	0.22	0.04	R _{co} 1	0.00	0.00
	R _{H2} 2	0.78	0.92	$R_{CO}2$	1.00	1.00
	$R_{H2}3$	0.00	0.00	R _{co} 3	0.00	0.00
	$R_{H2}4$	0.00	0.01	R _{CO} 4	0.00	0.00
	$R_{H2}5$	0.00	0.03	R _{co} 5	0.00	0.00
Apparent Activation Energy (eV)	_	1.47	0.86		0.71	0.53
Short Circuit Turnover Frequency (1/s)		2.64×10^{0}	5.29×10^{3}		2.52×10^{2}	7.53×10^{2}

In the case of CO oxidation, FeO₂-SrO surface displays a higher TOF than the FeO₂-LaO surface by a factor of three. For both surfaces, the DRC analysis (Table 2) indicates that the TOFs are entirely controlled by the formation of surface carbon dioxide (R_{CO} 2) and the free energy diagram (Figure 5) revealed that TS_{CO} 2 for FeO₂-LaO has a 0.10 eV higher free energy compared to that of FeO₂-SrO. Thus, the FeO₂-SrO surface exhibits a slightly higher TOF and lower apparent activation energy than the FeO₂-LaO surface. The apparent activation energies calculated for the CO oxidation process are lower by 0.76 and 0.33 eV than the ones calculated for H₂ oxidation process over FeO₂-LaO and FeO₂-SrO surfaces, respectively. However, the calculated short circuit TOF for the H₂ oxidation process on the FeO₂-SrO surface at a temperature of 1073 K is an order of magnitude higher than the TOFs predicted for CO oxidation process over both surfaces.

Next, the effect of anode potential bias on the fuel oxidation process is examined for H₂, CO, and syngas fuels since a potential bias can alter the reaction free energies and activation barriers of elementary reactions that involve a charge transfer process. Here, we followed a similar methodology used in our earlier work on the SFMO double perovskite ²⁴. As described earlier, the open-circuit potential (OCP) for H₂ and CO oxidation reactions are calculated as 1.1 V and we specify this value as our reference potential for the cathode. The possibilities of 0, 1, or 2 e⁻ charge transfer for a given elementary step are included in the microkinetic model. The free

energies of elementary steps that involve charge transfer are shifted by the amount of charge multiplied by the cell voltage (ΔV) and these corrections to the free energy of reaction (ΔG_i^{rxn}) and activation barrier (ΔG_i^{\dagger}) are incorporated using the following expressions:

$$\Delta G_i^{rxn}(\Delta V) = \Delta G_i^{rxn}(\Delta V = 0) + n_i FV \tag{16}$$

$$\Delta G_i^{\dagger}(\Delta V) = \Delta G_i^{\dagger}(\Delta V = 0) + n_i F \beta V \tag{17}$$

where n_j refers to the number of electrons transferred in the elementary charge transfer step, F is the Faraday's constant, β refers to the symmetry factor of the elementary step, and ΔV is the cell potential in volts *i.e.*, cathode reference potential subtracted by anode potential such that $\Delta V = 0$ refers to the short circuit condition. Two possible values for the symmetry factor, $\beta = 0$ and $\beta = 0.5$ were used in the present study to describe fast charge transfer and charge transfer that occurs during a reaction step experiencing a solid phase interfacial potential, respectively 63 . Greater details on our anode biasing methodology for H_2 , CO, and syngas oxidation reactions are outlined in Section S4 of the Supporting Information. The elementary steps involved in this extended microkinetic model and the calculated rates for H_2 and CO electro-oxidation reactions at a representative cell voltage of 0.7 V are presented in Tables S1 and S2 of the Supporting Information. In the presence of syngas fuel, both H_2 and CO electro-oxidation reactions can occur together with the thermochemical water-gas shift (WGS) reaction as shown in Figure 6.

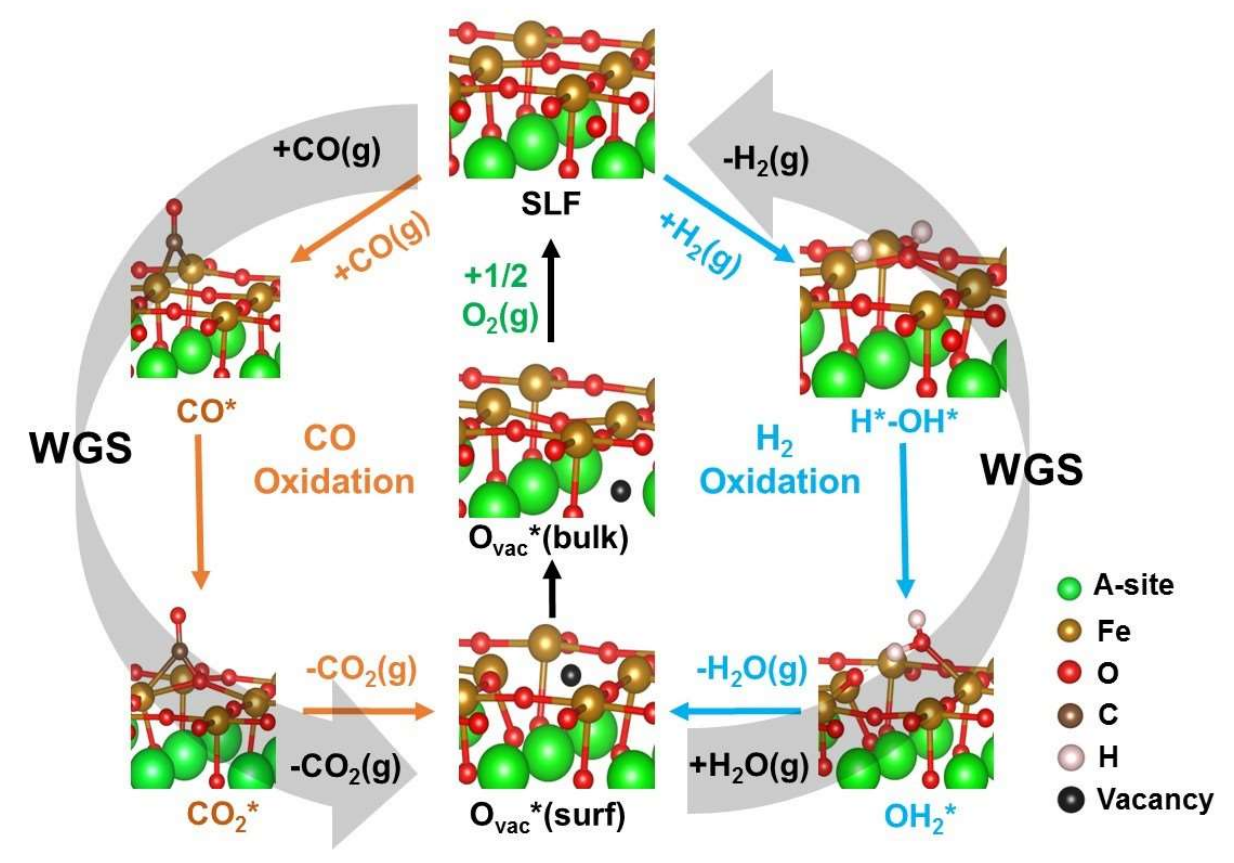


Figure 6: Proposed mechanism for syngas oxidation and water-gas shift (WGS) reaction on $SrLaFeO_{4-\delta}$ surface.

In the case of H_2 oxidation, the elementary reaction rates calculated with $\beta=0$ suggest that the possibilities of two-electron charge transfer during $R_{H2}2$ or $R_{H2}3$, and two one-electron charge transfers during $R_{H2}2$ and $R_{H2}3$ are all equally favorable on both surface models. However, the two-electron charge transfer during H_2O desorption process ($R_{H2}3$) is found to be more favorable compared to other possible charge transfer possibilities when β value is increased to 0.5. Similarly, the possibility of two-electron charge transfer during CO_2 desorption process ($R_{CO}3$) is found to be more favorable with $\beta=0.5$, whereas multiple possibilities of charge transfer became equally favorable when $\beta=0$ is used in the microkinetic model. While the overall TOFs calculated for the H_2 oxidation process at a cell voltage of 0.7 V ($\beta=0.5$) are decreased relative to short circuit conditions, the trends observed between the two SLF surfaces

are similar to short circuit conditions. For example, the calculated TOFs for H_2 and CO oxidation processes over the FeO₂-LaO surface at ΔV = 0.7 V are lower than the FeO₂-SrO surface for both β values. To visualize any changes in activity trends observed in the presence of anode bias potentials, we calculated the current densities at different cell voltages.

The current density (i in Acm⁻²) for a specific oxidation process is calculated using the relation, $i = zer\Gamma$, where z is the number of electron(s) involved in the reaction, r represents the calculated overall reaction rate or TOF (s⁻¹), and Γ is the number of active sites per surface area (cm⁻²). The number of active sites per surface is set as the inverse of the surface area of our SLF models $(1.39 \times 10^{-18} \text{ m}^2)$ for all fuels (e.g., one active site per surface model). The simulated polarization curves that reflect the kinetic relationship between the cell voltage and current density ($\beta = 0.5$) for H₂, CO, and syngas oxidation processes are displayed in Figure 7. It is to be noted here that this simulation does not incorporate mesoscale and macroscale effects such as molecular and pore diffusion effects and does not incorporate explicit cathodic kinetics. While the omission of ohmic loss and mass transfer limitations in our model could be somewhat justified because of high temperatures used in SOFC cells, these factors could affect the cell performance at relevant operating conditions and a quantitative prediction of experimental cell behavior cannot be obtained from this analysis. Nonetheless, this analysis is aimed at understanding the relative activity of different surfaces for different fuel oxidation processes and how the potential bias affects the activity and rate-limiting process of these surfaces.

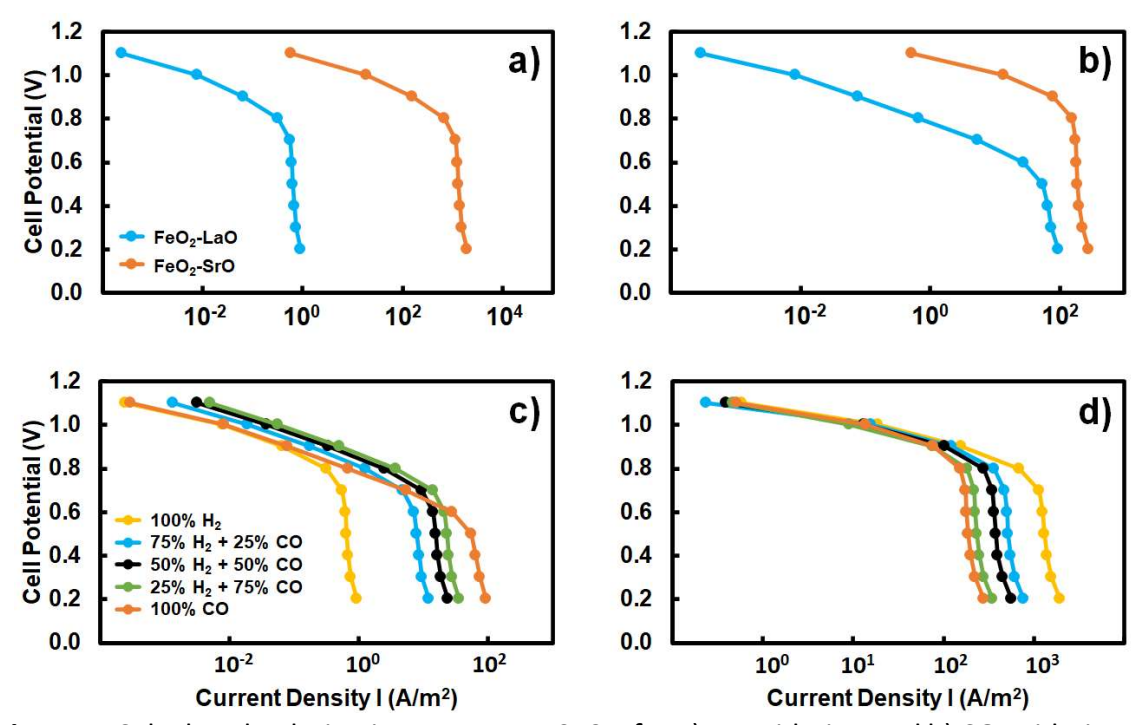


Figure 7: Calculated polarization curves at 1073 K for a) H_2 oxidation and b) CO oxidation on FeO₂-LaO (blue) and FeO₂-SrO (orange) surface models ($P_{H2,CO} = 1.00$ atm, $P_{H2O,CO2} = 0.03$ atm, and $P_{O2} = 0.21$ atm). (c-d) Calculated polarization curves for syngas oxidation at 1073 K on (c) FeO₂-LaO and (d) FeO₂-SrO surface models ($P_{H2,CO} = 1.00$ atm, $P_{H2O} = 0.03$ atm, $P_{CO2} = 0.003$ atm, and $P_{O2} = 0.21$ atm). β = 0.5 is used for all charge transfer reactions.

The polarization curves calculated for H_2 oxidation (Figure 7(a)) predicted higher current densities for the FeO₂-SrO surface than the FeO₂-LaO surface at all cell voltages which is consistent with the TOFs and apparent activation barriers predicted at short circuit conditions (Table 2). At a cell voltage of 0.7 V, the current densities for H_2 oxidation on the FeO₂-SrO surface are calculated as 0.27 (β = 0) and 0.11 (β = 0.5) A/cm² which are in the same order of magnitude reported by experimental studies (\sim 0.72 A/cm²) ¹⁴. Since the TOFs and apparent activation barriers calculated for CO oxidation at short circuit conditions are close for both surfaces, the current densities calculated for the FeO₂-LaO surface are also in the same order of magnitude with the FeO₂-SrO surface at cell voltages below 0.5 V (Figure 7(b)). However, 2-4 orders of magnitude higher current densities were observed for the FeO₂-SrO surface compared to the FeO₂-LaO surface at higher cell voltage conditions suggesting that there could be a change

in rate-limiting process for CO oxidation between low and high voltage conditions. Figures 7(cd) depict the syngas oxidation polarization curves for different ratios of syngas on the two FeO₂terminated surfaces. The syngas oxidation mechanism incorporates all elementary steps from both H₂ and CO oxidation reactions which implies the existence of a water-gas shift (WGS) thermochemical mechanism in addition to the electro-oxidation processes, as illustrated in Figure 6.. The rates calculated for individual reactions, such as H₂ electro-oxidation, CO electrooxidation, and WGS for different ratios of H₂:CO at a cell voltage of 0.7 V are summarized in Table S3 of the Supporting Information. On the FeO₂-LaO surface, the rates calculated for the CO electro-oxidation and WGS (producing H₂ and CO₂) are very similar and reverse H₂ electrooxidation was observed for all ratios of H₂:CO. Since this surface is more active for CO electrooxidation, the overall activity increases with increasing concentration of CO. H₂ electrooxidation was found to be an order of magnitude higher than CO oxidation on the FeO₂-SrO surface at different H₂:CO ratios which further promotes reverse WGS (producing H₂O and CO). Here, the overall activity increases with increasing concentration of H₂. The reverse WGS rates on FeO₂-SrO are higher than WGS rates of FeO₂-LaO for all H₂:CO ratios. The simulated polarization curves for the FeO₂-LaO surface (Figure 7(c)) display that the current density increases with increasing concentration of CO at low cell voltages since this surface exhibits higher activity towards CO oxidation at short circuit conditions. At cell voltages above 0.6 V, slightly higher current densities were observed for the syngas mixtures compared to pure H₂ or CO fuels for the FeO₂-LaO surface. On the FeO₂-SrO surface (Figure 7(d)), the current density increases with increasing concentration of H₂ at all cell voltages since H₂ electro-oxidation was found to be more favorable on this surface than CO electro-oxidation (Figures 6(a-b)). The calculated current densities for syngas (50% H₂ + 50% CO) oxidation on the FeO₂-SrO surface at a cell voltage of 0.7 V (0.09 (β = 0) and 0.04 (β = 0.5) A/cm²) are an order of magnitude lower than the experimental value (~ 0.27 A/cm²) ¹⁴. Overall, the electrochemical activity of SLF anodes in the presence of syngas fuel seems to originate mainly from the H₂ electro-oxidation over the FeO₂-SrO surface and CO₂ is chemically reduced to CO via WGS which also produces H₂O.

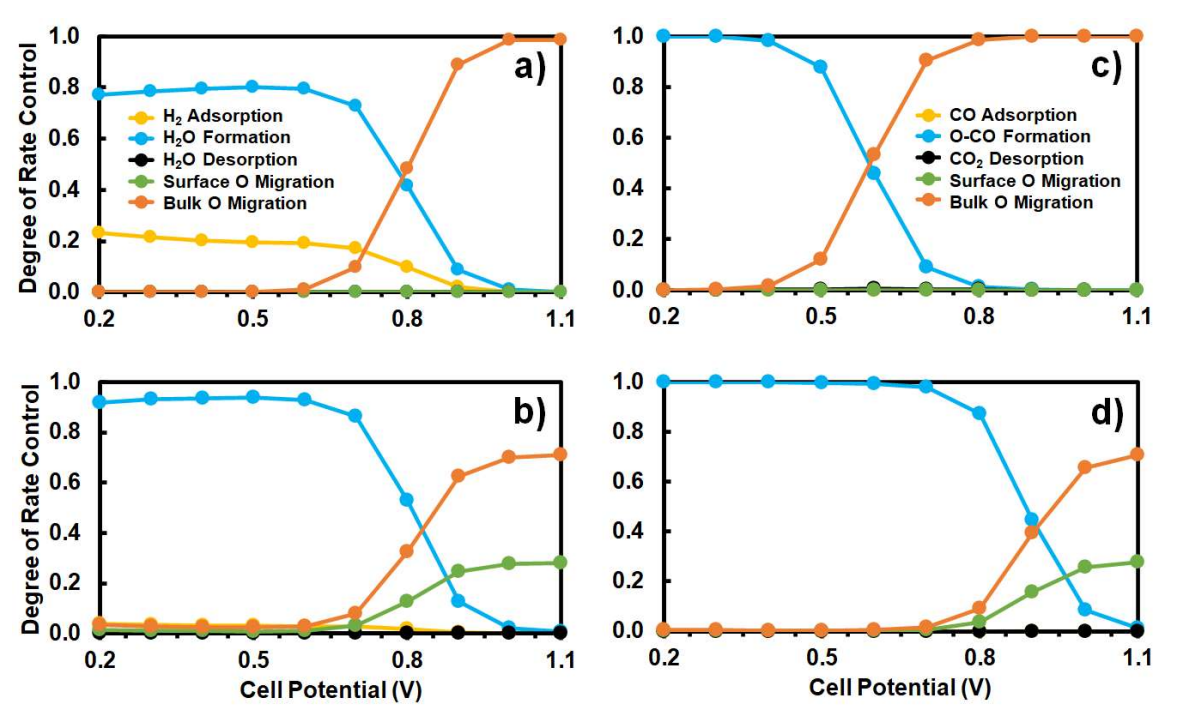


Figure 8: Degree of rate control (DRC) analysis for H_2 oxidation on a) FeO_2 -LaO and b) FeO_2 -SrO surfaces and degree of rate control for CO oxidation on c) FeO_2 -LaO and d) FeO_2 -SrO surfaces as a function of cell potential (T = 1073 K; $P_{H_2,CO}$ = 1.00 atm, P_{H_2,CO_2} = 0.03 atm, and P_{O_2} = 0.21 atm).

To understand the polarization behavior of SLF anodes for the H_2 and CO electrooxidation processes, we calculated the degree of rate control with respect to cell potential as displayed in Figure 8. The overall rates and degrees of rate control are summarized at a representative cell voltage of 0.7 V in Table S4 of the Supporting Information. In accordance with the short-circuit analysis, the H_2O formation process (R_{H2} 2) is mainly rate-limiting for H_2 oxidation at cell voltages < 0.8 V for both surfaces, whereas the bulk oxygen migration process (R_{H2} 5) becomes dominantly rate-controlling at higher cell voltage conditions (Figures 8 (a-b)).

This change in rate-limiting step is reflected in the logarithmic polarization curves presented in Figure 7(a) for the H₂ electro-oxidation. Since our analysis with $\beta = 0.5$ suggested that the charge transfer occurs only in R_{H2} 3 which involves H_2O desorption and surface vacancy formation, the current density did not change much with the cell potential where R_{H2} 2 is rate-limiting in the regime of $\Delta V < 0.8 \text{ V}$. Logarithmic changes in current density with high cell potentials are observed in the regime of $\Delta V > 0.8 \text{ V}$ where the rate-limiting oxide migration process occurs after the charge transfer process. Similarly, the rate-controlling process changes from CO₂ formation (R_{CO} 2) at low cell voltages (< 0.6 V) to bulk oxygen migration (R_{CO} 5) at Δ V > 0.6 V for CO electro-oxidation on the FeO₂-LaO surface (Figure 8(c)), whereas such change in the rate-limiting process is observed only above 0.9 V for the FeO₂-SrO surface (Figure 8(d)). This trend is reflected in the polarization curves in Figure 7(b) where logarithmic current density is observed above 0.6 V for the FeO₂-LaO surface and the current density remains nearly constant until 0.9 V for the FeO₂-SrO surface. This is again consistent with the rate-limiting processes occurring before and after the charge transfer process $(R_{CO}3)$ in these different regimes. These results suggest that the overall performance of SLF anodes can be improved by identifying ways to reduce the surface H₂O/CO₂ formation and bulk oxygen diffusion barriers. For example, bulk SLF doping could decrease vacancy-mediated transport barriers and exsolvation strategies could decrease reactions barriers for key oxidation elementary steps and increase the anode electronic conductivity.

3.5 Effect of B-Site Doping on the SLF Oxidation Activity

Substitutional dopants are commonly used to improve the performance of MIEC materials since dopants can alter the electronic, ionic, and catalytic properties of the parent

material. Here, we conducted a preliminary analysis of the effects of substitutional doping of the SLF surface models on the H_2 oxidation activity by replacing a surface Fe atom (active site Fe atom, $*_{Fe}-O$) by various dopants such as Co, Ni, and Mn. Our microkinetic analysis for the non-doped SLF surface models predicted that the H_2O formation process is mainly rate-controlling at short circuit and low voltage conditions for H_2 oxidation, whereas the bulk oxide migration becomes rate-controlling at high voltage conditions. While substitutional doping of bulk SLF can improve the bulk oxygen diffusion barrier by increasing the concentration of vacancy defects 35,64 , a careful analysis is necessary to identify appropriate dopant elements and effective doping ratios as well as elucidation of the diffusion mechanism which are all beyond the scope of this study. Here, we focused on strategies to modulate surface H_2O formation activity that could improve the H_2 oxidation activity of SLF materials at low cell voltage conditions.

Table 3: Transition state free energies of the dissociative adsorption of hydrogen (ΔG^{\ddagger}_{H2} in eV) and surface water formation ($\Delta G^{\ddagger}_{H2O}$ in eV) at 1073 K, P_{H2} (gas) = 1.0 atm, P_{H2O} (gas) = 0.03 atm, and P_{O2} (gas) = 0.21 atm) calculated with reference to the energies of initial active site and H_2 gas, and turnover frequency (TOF in s⁻¹) of H_2 oxidation calculated at short circuit conditions for single surface metal atom doped $Fe_{1-x}M_xO_2$ -LaO and $Fe_{1-x}M_xO_2$ -SrO (x = 0.11; M = Fe, Co, Ni, Mn) surface models.

ΔG [‡] _{H2} (eV)		ΔG [‡] _{H2}	_{:o} (eV)	Short Circu	Short Circuit TOF (s ⁻¹)		
Dopant	Fe _{1-x} M _x O ₂	Fe _{1-x} M _x O ₂	Fe _{1-x} M _x O ₂	$Fe_{1-x}M_xO_2$	Fe _{1-x} M _x O ₂	$Fe_{1-x}M_xO_2$	
(M)	-LaO	-SrO	-LaO	-SrO	-LaO	-SrO	
Fe	2.60	1.89	2.73	2.21	2.64×10^{0}	5.29×10^{3}	
Со	1.39	1.09	1.71	-0.07	9.41×10^{3}	8.29×10^{2}	
Ni	1.58	2.39	2.43	1.75	8.65×10^{1}	2.10×10^{1}	
Mn	1.85	2.23	2.28	1.87	3.79×10^{2}	6.81×10^{2}	

The free energies of the TSs corresponding to H_2 dissociation ($TS_{H2}1$) and H_2O formation process ($TS_{H2}2$) together with the TOFs calculated at short circuit conditions for the two doped surface models, $Fe_{1-x}M_xO_2$ -LaO and $Fe_{1-x}M_xO_2$ -SrO (x=0.11; M=Fe, Co, Ni, Mn)

are presented in Table 3 and the corresponding free energy diagrams are illustrated in Figures S2 and S3 of the Supporting Information. In the case of the Fe_{1-x}M_xO₂-LaO surface, our calculations indicate that the rate-controlling $TS_{H2}2$ is stabilized in the presence of dopants and consequently, the TOFs increase relative to the non-doped FeO₂-LaO surface. This indicates that Fe-site doping is a prudent strategy to improve the overall activity of SLF by making the FeO₂-LaO surface more viable for H₂ oxidation. Among the dopants considered here, Co displays the lowest free energy pathway for H₂ oxidation (Figure S2 in the Supporting Information) and the TOFs calculated for these dopants are 3 orders of magnitude higher than the non-doped FeO₂-LaO surface and are in the same order of magnitude calculated for the non-doped FeO₂-SrO surface. For the Fe_{1-x}M_xO₂-SrO surface (Figure S3 in the Supporting Information), dopants exhibited lower TOFs compared to the non-doped FeO₂-SrO surface (Table 3). This trend indicates a change in rate-controlling step for the FeO₂-SrO surface in the presence of dopants. The free energy profiles presented in Figure S3 reveal that the TSs corresponding to H₂ dissociation $(TS_{H2}1)$ are higher in energy compared to $TS_{H2}2$ for all the dopants and the surface vacancy structures $(*_M - V_O(S), IM_{H2}4)$ are significantly stabilized compared to FeO₂-SrO. Thus, our microkinetic model predicted a high surface coverage of $IM_{H2}4$ for all the dopants (> 99% for Co). Consequently, rate-control analysis indicated that greater than 90% of the rate is controlled by bulk oxide migration $(R_{H2}5)$ process for all the dopants considered here. The highly stable surface vacancy structures observed for the doped Fe_{1-x}M_xO₂-SrO surface models further suggest that the catalytic cycle for fuel oxidation over these surfaces could involve multiple oxygen vacancies which is not considered in our preliminary analysis. Despite this limitation, we examined the thermodynamic favorability of doping for both surface models with the following equation.

$$FeO_2 - LaO + Fe_{1-x}M_xO_2 - SrO \rightarrow FeO_2 - SrO + Fe_{1-x}M_xO_2 - LaO$$
 (18)
 $(x = 0.11; M = Co, Ni, Mn)$

Co, Ni, and Mn display a reaction free energy (ΔG^{rxn}) of -0.77, -0.23, and -0.49, respectively suggesting that a combined presence of doped FeO₂-LaO surface with non-doped FeO₂-SrO surface is thermodynamically more favorable. Hence, the activity of SLF anodes is increased in the presence of all dopants as the more active doped FeO₂-LaO surfaces coexist with the highly active FeO₂-SrO surface. This combined effect increases the net number of active sites for doped SLF anodes, especially for the Co dopant. Overall, this analysis suggests that the H₂ oxidation activity of the FeO₂-LaO surfaces could be improved by doping with Co, Mn, and Ni. The activity of the FeO₂-SrO surface is decreased with dopant introduction due to a change in the rate-determining step and a high driving force for the formation of surface vacancies. Among the three dopants, Co could yield the best performance.

3.6 Effect of Sulfur Poisoning on the activity of SLF

The experimental literature indicated that the SLF-based anodes exhibit high tolerance to sulfur and the fuel oxidation activity does not diminish in the presence of H₂S ^{14,15}. In this work, we used constrained *ab* initio thermodynamics analysis to investigate the sulfur poisoning mechanism of doped and non-doped SLF surface models under SOFC operating conditions with the aim of understanding the limits of sulfur stability on these materials. As proposed earlier by Walker et. al. for the SFMO material ²⁸, two different mechanisms were considered for the interaction of sulfur with the SLF surfaces, namely, dissociative adsorption of H₂S on the SLF surface, and replacement of surface oxygen by sulfur (Figure 9).

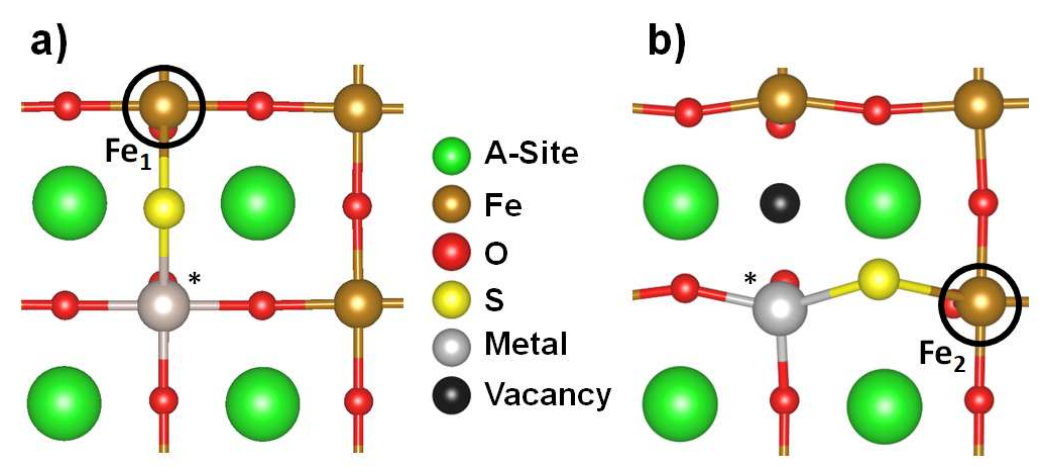


Figure 9: Top views of optimized structures of a) sulfur adsorbed on the oxygen vacancy ($H_2S + M-V_0^{\bullet\bullet}-Fe_1 \leftrightarrow H_2 + M-S-Fe_1$, M = Fe, Co, Ni, Mn) and b) sulfur replacing surface oxygen ($H_2S + M-O_0^{\bullet\bullet}-Fe_2 \leftrightarrow H_2O + M-S-Fe_2$, M = Fe, Co, Ni, Mn), respectively.

The H₂S dissociative adsorption reaction can be described as

$$H_2S(g) + M - V_0^{"} - Fe_1 \rightarrow H_2(g) + M - S - Fe_1(M = Fe, Co, Ni, Mn)$$
 (19)

The corresponding dissociative adsorption reaction free energy (ΔG^{ads}) is calculated by the following expression,

$$\Delta G^{ads} = (E_{H2}^{DFT} + \mu_{H2}) + E_{M-S-F_1}^{DFT+U} - (E_{H2S}^{DFT} + \mu_{H2S}) - E_{M-V_0-Fe_1}^{DFT+}$$
 (20)

The oxide replacement reaction is described as

$$H_2S(g) + M - O - Fe_2 \rightarrow H_2O(g) + M - S - Fe_2 (M = Fe, Co, Ni, Mn)$$
 (21)

and the corresponding replacement reaction free energy (ΔG^{repl}) is calculated by the following expression,

$$\Delta G^{repl} = (E_{H2O}^{DFT} + \mu_{H2O}) + E_{M-S-Fe_2}^{DFT+U} - (E_{H2S}^{DFT} + \mu_{H2S}) - E_{M-O-Fe_2}^{DFT+U}$$
 (22)

 Fe_1 refers to the surface Fe atom that is directly connected to the oxygen vacancy where sulfur is adsorbed and Fe_2 is bonded to the surface oxygen that is replaced by sulfur (Figure 9). While both mechanisms produce surface sulfur, these sulfur atoms can have different effects on the proposed catalytic cycles of H_2 and CO oxidation. The dissociative adsorption process fills the native surface V_0° with sulfur blocking the adsorption site for H_2 and CO, whereas the oxygen

replacement mechanism replaces one of the neighboring surface oxygens that is involved in the formation of surface H₂O and CO₂; thus, this mechanism could affect the kinetic barriers for these reactions.

Table 4: Reaction free energies for the dissociative adsorption of H_2S (ΔG^{ads} in eV, eq 20) and oxygen replacement reaction (ΔG^{repl} in eV, eq 22) for the $Fe_{1-x}M_xO_2$ -LaO and $Fe_{1-x}M_xO_2$ -SrO (x= 0.11; M = Fe, Co, Ni, Mn) surface models calculated at T = 1073 K, C_{H2S} = 50 PPM, P_{H2} = 1 atm, and P_{H2O} = 0.03 atm.

	Fe _{1-x} M _x O ₂ -LaO			Fe _{1-x} M _x O ₂ -SrO		
Dopant (M)	ΔG^{ads} (eV)	ΔG^{repl} (eV)		ΔG^{ads} (eV)	ΔG ^{repl} (eV)	
Fe	1.73	1.09	_	2.94	0.16	
Со	2.25	0.01		1.74	0.61	
Ni	4.04	-0.08		3.05	1.46	
Mn	1.82	0.75		2.10	-0.15	

The free energies of sulfur adsorption and oxide replacement reactions (Table 4) calculated with a H_2S concentration of 50 ppm 14 suggest that the sulfur adsorption process is in general less favorable than the oxide replacement process for all the dopants on the two surface models. While the oxide replacement reaction is still highly unfavorable on the non-doped FeO₂-LaO surface ($\Delta G^{repl} = 1.09 \text{ eV}$), this reaction is endergonic only by 0.16 eV on FeO₂-SrO surface. Further calculations indicate that the accumulation of sulfur on the FeO₂-SrO surface via oxide replacement reaction is possible when the H_2S concentration increases above 290 PPM at a temperature of 1073 K. However, this amount is much larger than the H_2S concentration that normally poisons Ni/YSZ (< 15 ppm) 4 suggesting that the SLF anodes are less susceptible for sulfur poisoning at concentrations of H_2S practical to SOFC conditions.

The free energies of the oxide replacement reaction on the FeO₂-LaO surface decrease in the presence of dopants and the least stable dopants were Co and Ni which are nearly in equilibrium with a ΔG^{repl} of 0.01 and -0.08 eV, respectively. On the other hand, the introduction of dopants on the FeO₂-SrO surface increase the free energies of oxide replacement reaction except for Mn for which an exergonic ΔG^{repl} of -0.15 eV was predicted by our calculations. As

discussed earlier in Section 3.5, substitutional doping of Co and Ni on the FeO₂-LaO surface increases the TOFs for H₂ oxidation on this surface (Table 3); however, one of the active oxygen atoms involved in surface water formation could be replaced by sulfur when the H₂S concentration in the fuel becomes higher than 56 and 20 ppm, respectively. This could have a negative impact on the oxidation activity. Mn increases the TOF for H₂ oxidation on the FeO₂-LaO surface and displays resistance to oxide replacement with sulfur for H₂S concentrations below 1.7 × 10⁵ ppm. In the case of FeO₂-SrO surface, the oxide replacement reaction on the Mn-doped surface becomes feasible when the H₂S concentration is > 10 ppm at 1073 K suggesting that Mn doping has negative effect on sulfur resistance on the more active surface. An overall comparison of H₂ oxidation TOFs (Table 3) and free energies of sulfur poisoning mechanisms (Table 4) reveals that doping with Co could improve activity on FeO₂-LaO surface, maintain adequate performance on the FeO₂-SrO surface, and displays sulfur resistance above the Ni/YSZ instability H₂S concentrations.

4. Conclusions

The activity of SLF based anode materials in the presence of H₂, CO, and syngas fuels was investigated using DFT + U theory and microkinetic modeling techniques. We constructed two representative FeO₂-terminated SLF (001) surface models with different underlying rocksalt (LaO and SrO) layers to examine the catalytic activity under anodic SOFC conditions.

Microkinetic analysis performed under short circuit conditions indicated that the FeO₂-SrO surface is more active for both H₂ and CO oxidation. In the presence of anode bias potential, a similar trend was observed at all cell voltage conditions. However, the CO oxidation activity of the FeO₂-SrO surface shifts from logarithmic scaling below cell voltages of 0.8 V such that the

FeO₂-LaO surface activity only differs from the FeO₂-SrO activity by a factor of three at short circuit conditions. Kinetic rate control analysis revealed that the key rate-limiting step changes from surface H₂O/CO₂ formation at low cell voltage conditions to bulk oxygen migration at high voltage conditions for these oxidation processes on both surface models. The CO electro-oxidation activity of SLF surfaces is found to be 1-2 orders of magnitude lower than the H₂ electro-oxidation activity. Syngas oxidation incorporates elementary steps from both H₂ and CO electro-oxidation reactions implying the existence of the thermochemical WGS reaction. For the active FeO₂-SrO surface, syngas oxidation derives its current density from H₂ oxidation and CO₂ is thermochemically reduced to CO via reverse WGS.

Next, we conducted a preliminary analysis of the introduction of surface B-site dopants on the SLF surface models to understand the effect of dopants on the H₂ oxidation activity at short circuit conditions. The free energy of rate-limiting H₂O formation TS on the FeO₂-LaO surface decreased and consequently, an increase in TOF was observed for all dopants. For the Co dopant, it exhibited 3 orders of magnitude higher TOF than the non-doped surface. While a similar trend in the free energy of H₂O formation TS was observed on the FeO₂-SrO surface with the introduction of dopants, the calculated TOFs for the doped surfaces were found to be lower than the non-doped surface. Since doping significantly stabilizes the surface vacancy structure on the FeO₂-SrO surface, the oxidation reaction was found to be rate-controlled by bulk oxygen diffusion rather than the surface H₂O formation process. A thermodynamic analysis of surface dopant formation indicates the favorability of more active doped FeO₂-LaO surfaces coexisting with the highly active non-doped FeO₂-SrO surface such that the number of active sites is increased in the presence of dopants. Lastly, we analyzed the sulfur poisoning mechanism of SLF surface models by examining the dissociative adsorption of H₂S and the replacement of

surface oxygen by sulfur. The dissociative adsorption of H2S reaction was found to be endergonic under SOFC operating conditions in the presence of 50 ppm of H₂S for all the doped and non-doped SLF surfaces which is consistent with the sulfur tolerance observed by experimental studies. In the cases of $Fe_{1-x}M_xO_2$ -LaO (x = 0.11; M = Co and Ni) and $Fe_{1-x}Mn_xO_2$ -SrO (x = 0.11) surfaces, lower free energies (-0.2 to 0.1 eV) calculated for the oxide replacement reactions suggest that the oxidation activity of these surfaces could be affected in the presence of slightly higher H₂S concentrations. Overall, SLF anodes exhibit reasonably good activity and sulfur resistance in the presence of H₂, CO, and syngas fuels and Co doping on the SLF surfaces seems to improve and/or maintain the catalytic activity of SLF while maintaining sulfur tolerance. Future work will focus on the effect of B-site doping on the bulk oxygen diffusion barrier to help the design of SLF based materials for direct use in SOFCs. Lastly, SLF-based anodes could have an impact on future hydrogen storage applications as an electrolysis material for H₂ generation or for energy generation in direct hydrocarbon fuel cells under sulfurcontaining conditions with the help of prudent doping strategies as determined by experimental and ab initio studies.

Supporting Information

The Supporting Information is available free of charge via the Internet at http://pubs.acs.org.

• Computational methodology for free energies of all gaseous and adsorbate species.

Estimation of bulk vacancy-mediated migration energy. Estimation of surface vacancy concentration under different oxygen chemical potentials. Computational methodology for the microkinetic modeling of thermochemical and anode biasing conditions for H₂, CO, and syngas fuels. Turnover rates of all elementary steps under anode biasing for H₂ and CO fuels. Turnover rates of syngas oxidation and thermochemical water-gas shift

under different H₂:CO ratios. Free energy diagrams of FeO₂-LaO and FeO₂-SrO doped

surfaces with Co, Ni, and Mn.

XYZ coordinates of intermediate and transition state structures calculated for the

electrochemical oxidation of H₂ and CO Fuels on the SrLaFeO₄ surface models.

Acknowledgments

This work was supported by the National Science Foundation under Grant No. DMR- 1832809

and partially supported by the South Carolina Smart State Center for Strategic Approaches to the

Generation of Electricity (SAGE). Computing resources are provided by the U.S. Department of

Energy facility located at National Energy Research Scientific Computing Center (NERSC)

under Contract No. DE-AC02-05CH11231 and ACCESS facilities located at Texas Advanced

Computing Center (TACC), San Diego Supercomputer Center (SDSC), and Purdue University

(grand no. TG-CTS090100). Finally, computing resources provided by the University of South

Carolina's High Performance Computing (HPC) group are gratefully acknowledged.

Author Information

Corresponding Author

*Email: heyden@cec.sc.edu

Author Contributions

All authors have given approval to the final version of the manuscript.

Notes

The authors declare no competing financial interest.

38

References

- (1) Steele, B. C. H.; Heinzel, A. Materials for Fuel-Cell Technologies. *Nature*, **2001**, *414*, 345–352. https://doi.org/10.1038/35104620.
- (2) McIntosh, S.; Gorte, R. J. Direct Hydrocarbon Solid Oxide Fuel Cells. *Chem Rev.*, **2004**, *104* (10), 4845–4865. https://doi.org/10.1021/cr020725g.
- (3) Wachsman, E. D.; Lee, K. T. Lowering the Temperature of Solid Oxide Fuel Cells. *Science*, **2011**, *334* (6058), 935–939. https://doi.org/10.1126/science.1204090.
- (4) Shri Prakash, B.; Senthil Kumar, S.; Aruna, S. T. Properties and Development of Ni/YSZ as an Anode Material in Solid Oxide Fuel Cell: A Review. *Renew. and Sustain. Energy Rev.*, 2014, 36, 149–179. https://doi.org/10.1016/j.rser.2014.04.043.
- (5) Fallah Vostakola, M.; Amini Horri, B. Progress in Material Development for Low-Temperature Solid Oxide Fuel Cells: A Review. *Energies*, **2021**, *14* (5), 1280. https://doi.org/10.3390/en14051280.
- (6) Tao, S.; Irvine, J. T. S. A Redox-Stable Efficient Anode for Solid-Oxide Fuel Cells. *Nat. Mater.*, **2003**, *2* (5), 320–323. https://doi.org/10.1038/nmat871.
- (7) Liu, Q.; Yang, C.; Dong, X.; Chen, F. Perovskite Sr₂Fe_{1.5}Mo_{0.5}O_{6-δ} as Electrode Materials for Symmetrical Solid Oxide Electrolysis Cells. *Int. J. Hydrog. Energy*, **2010**, *35* (19), 10039–10044. https://doi.org/10.1016/j.ijhydene.2010.08.016.
- (8) Liu, Q.; Dong, X.; Xiao, G.; Zhao, F.; Chen, F. A Novel Electrode Material for Symmetrical SOFCs. *Adv. Mater.*, **2010**, *22* (48), 5478–5482. https://doi.org/10.1002/adma.201001044.
- (9) Ruddlesden, S. N.; Popper, P. New Compounds of the K₂NiF₄ Type. *Acta Crystallogr.*, **1957**, *10*, 538–539. https://doi.org/10.1107/s0365110x57001929.
- (10) Takeguchi, T.; Yamanaka, T.; Takahashi, H.; Watanabe, H.; Kuroki, T.; Nakanishi, H.; Orikasa, Y.; Uchimoto, Y.; Takano, H.; Ohguri, N.; Matsuda, M.; Murota, T.; Uosaki, K.; Ueda, W. Layered Perovskite Oxide: A Reversible Air Electrode for Oxygen Evolution/Reduction in Rechargeable Metal-Air Batteries. *J. Am. Chem. Soc.*, **2013**, *135* (30), 11125–11130. https://doi.org/10.1021/ja403476v.
- (11) Zhao, H.; Mauvy, F.; Lalanne, C.; Bassat, J.; Fourcade, S.; Grenier, J. New Cathode Materials for ITSOFC: Phase Stability, Oxygen Exchange and Cathode Properties of La_{2-x}NiO_{4+δ}. Solid State Ion., 2008, 179 (35–36), 2000–2005. https://doi.org/10.1016/j.ssi.2008.06.019.
- (12) Cao, Y.; Liang, J.; Li, X.; Yue, L.; Liu, Q.; Lu, S.; Asiri, A. M.; Hu, J.; Luo, Y.; Sun, X. Recent Advances in Perovskite Oxides as Electrode Materials for Supercapacitors. *Chem. Commun.*, **2021**, *57*, 2343-2355. https://doi.org/10.1039/d0cc07970g.
- (13) Li, X.; Zhao, H.; Liang, J.; Luo, Y.; Chen, G.; Shi, X.; Lu, S.; Gao, S.; Hu, J.; Liu, Q.; Sun, X. A-Site Perovskite Oxides: An Emerging Functional Material for Electrocatalysis and

- Photocatalysis. *J. Mater. Chem. A*, **2021**, *9*, 6650–6670. https://doi.org/10.1039/d0ta09756j.
- (14) Xu, L.; Yin, Y.-M.; Zhou, N.; Wang, Z.; Ma, Z.-F. Sulfur Tolerant Redox Stable Layered Perovskite SrLaFeO_{4-δ} as Anode for Solid Oxide Fuel Cells. *Electrochem. Commun.*, **2017**, 76, 51–54. https://doi.org/10.1016/j.elecom.2017.01.017.
- (15) Wang, Z.; Yin, Y.-M.; Yu, Y.; Song, Y.; Ma, Z.-F.; Yin, J. Roles of Fe Ni Nanoparticles and SrLaFeO₄ Substrate in the Performance and Reliability of a Composite Anode Prepared through In-Situ Exsolution for Intermediate Temperature Solid Oxide Fuel Cells (I). *Int. J. Hydrog. Energy*, **2018**, *43* (22), 10440–10447. https://doi.org/10.1016/j.ijhydene.2018.04.090.
- (16) Wu, N.; Wang, W.; Zhong, Y.; Yang, G.; Qu, J.; Shao, Z. Nickel-Iron Alloy Nanoparticle-Decorated K₂NiF₄-Type Oxide as an Efficient and Sulfur-Tolerant Anode for Solid Oxide Fuel Cells. *ChemElectroChem*, **2017**, *4* (9), 2378–2384. https://doi.org/10.1002/celc.201700211.
- (17) Chang, H.; Chen, H.; Shao, Z.; Shi, J.; Bai, J.; Li, S.-D. In Situ Fabrication of (Sr,La)FeO₄ with CoFe Alloy Nanoparticles as an Independent Catalyst Layer for Direct Methane-Based Solid Oxide Fuel Cells with a Nickel Cermet Anode. *J. Mater. Chem. A*, **2016**, *4* (36), 13997—14007. https://doi.org/10.1039/C6TA04639H.
- (18) Park, S.; Han, H.; Choi, J.; Lee, S.; Park, M.; Kim, W. B. Ruddlesden–Popper Oxide (La_{0.6}Sr_{0.4})₂(Co,Fe)O₄ with Exsolved CoFe Nanoparticles for a Solid Oxide Fuel Cell Anode Catalyst. *Energy Technol.*, **2021**, *9* (7), 2100116. https://doi.org/10.1002/ente.202100116.
- (19) Li, H.; Song, Y.; Xu, M.; Wang, W.; Ran, R.; Zhou, W.; Shao, Z. Exsolved Alloy Nanoparticles Decorated Ruddlesden–Popper Perovskite as Sulfur-Tolerant Anodes for Solid Oxide Fuel Cells. *Energy Fuels*, **2020**, *34* (9), 11449–11457. https://doi.org/10.1021/acs.energyfuels.0c02228.
- (20) Chung, Y. S.; Kim, T.; Shin, T. H.; Yoon, H.; Park, S.; Sammes, N. M.; Kim, W. B.; Chung, J. S. In Situ Preparation of a La_{1.2}Sr_{0.8}Mn_{0.4}Fe_{0.6}O₄ Ruddlesden–Popper Phase with Exsolved Fe Nanoparticles as an Anode for SOFCs. *J. Mater. Chem. A*, **2017**, *5* (14), 6437–6446. https://doi.org/10.1039/c6ta09692a.
- (21) Tan, W.; Huan, D.; Yang, W.; Shi, N.; Wang, W.; Peng, R.; Wu, X.; Lu, Y. A First-Principles Study on Divergent Reactions of Using a Sr₃Fe₂O₇ Cathode in Both Oxygen Ion Conducting and Proton Conducting Solid Oxide Fuel Cells. *RSC Adv.* **2018**, *8* (47), 26448–26460. https://doi.org/10.1039/C8RA04059A.
- (22) Zhou, J.; Chen, G.; Wu, K.; Cheng, Y. Interaction of La₂NiO₄ (100) Surface with Oxygen Molecule: A First-Principles Study. *J. Phys. Chem. C*, **2013**, *117* (25), 12991–12999. https://doi.org/10.1021/jp403094x.
- (23) Akbay, T.; Staykov, A.; Druce, J.; Téllez, H.; Ishihara, T.; Kilner, J. A. The Interaction of Molecular Oxygen on LaO Terminated Surfaces of La₂NiO₄. *J. Mater. Chem. A*, **2016**, *4* (34), 13113–13124. https://doi.org/10.1039/C6TA02715F.

- (24) Suthirakun, S.; Ammal, S. C.; Muñoz-García, A. B.; Xiao, G.; Chen, F.; zur Loye, H.-C.; Carter, E. A.; Heyden, A. Theoretical Investigation of H₂ Oxidation on the Sr₂Fe₁.₅Mo₀.₅O₆ (001) Perovskite Surface under Anodic Solid Oxide Fuel Cell Conditions. *J. Am. Chem. Soc.*, **2014**, 136 (23), 8374–8386. https://doi.org/10.1021/ja502629j.
- (25) Han, Z.; Dong, H.; Wu, Y.; Yang, Y. Locating the Rate-Limiting Step of Hydrogen Conversion on Sr₂Fe_{1.5}Mo_{0.5}O₆ (001) Surface: Implications for Efficient SOFC Anode Design. *Appl. Surf. Sci.*, **2022**, *595*, 153513. https://doi.org/10.1016/j.apsusc.2022.153513.
- (26) Ren, B.; Croiset, E.; Ricardez–Sandoval, L. A Theoretical Study on CO₂ Electrolysis through Synergistic Manipulation of Ni/Mn Doping and Oxygen Vacancies in La(Sr)FeO₃. *J. Catal.*, **2020**, *383*, 273–282. https://doi.org/10.1016/j.jcat.2020.01.033.
- (27) Ammal, S. C.; Heyden, A. Reaction Kinetics of the Electrochemical Oxidation of CO and Syngas Fuels on a $Sr_2Fe_{1.5}Mo_{0.5}O_{6-\delta}$ Perovskite Anode. *J. Mater. Chem. A.*, **2015**, *3* (43), 21618–21629. https://doi.org/10.1039/C5TA05056A.
- (28) Walker, E.; Ammal, S. C.; Suthirakun, S.; Chen, F.; Terejanu, G. A.; Heyden, A. Mechanism of Sulfur Poisoning of Sr₂Fe_{1.5}Mo_{0.5}O_{6-δ} Perovskite Anode under Solid Oxide Fuel Cell Conditions. *J. Phys. Chem. C*, **2014**, *118* (41), 23545–23552. https://doi.org/10.1021/jp507593k.
- (29) Kresse, G.; Furthmüller, J. Efficient Iterative Schemes for Ab Initio Total-Energy Calculations Using a Plane-Wave Basis Set. *Phys. Rev. B*, **1996**, *54* (16), 11169–11186. https://doi.org/10.1103/PhysRevB.54.11169.
- (30) Joubert, D. From Ultrasoft Pseudopotentials to the Projector Augmented-Wave Method. *Phys. Rev. B*, **1999**, *59* (3), 1758–1775. https://doi.org/10.1103/PhysRevB.59.1758.
- (31) Perdew, J. P.; Yue, W. Accurate and Simple Density Functional for the Electronic Exchange Energy: Generalized Gradient Approximation. *Phys. Rev. B*, **1986**, *33* (12), 8800–8802. https://doi.org/10.1103/PhysRevB.33.8800.
- (32) Perdew, J. P.; Wang, Y. Accurate and Simple Analytic Representation of the Electron-Gas Correlation Energy. *Phys. Rev. B*, **1992**, *45* (23), 13244-13249. https://doi.org/10.1103/PhysRevB.98.079904.
- (33) Dudarev, S. L.; Botton, G. A.; Savrasov, S. Y.; Humphreys, C. J.; Sutton, A. P. Electron-Energy-Loss Spectra and the Structural Stability of Nickel Oxide: An LSDA+U Study. *Phys. Rev. B*, **1998**, *57* (3), 1505–1509. https://doi.org/10.1103/PhysRevB.57.1505.
- Ota, T.; Kizaki, H.; Morikawa, Y. Mechanistic Analysis of Oxygen Vacancy Formation and Ionic Transport in Sr₃Fe₂O_{7-δ}. *J. Phys. Chem. C*, **2018**, *122* (8), 4172–4181. https://doi.org/10.1021/acs.jpcc.7b11904.
- (35) Szaro, N. A.; Ammal, S. C.; Chen, F.; Heyden, A. An Ab Initio Study of the Oxygen Defect Formation and Oxide Ion Migration in (Sr_{1-x}Pr_x)₂FeO_{4±δ}. *J. Power Sources*, **2021**, *515*, 230602. https://doi.org/10.1016/j.jpowsour.2021.230602.

- (36) Jain, A.; Ong, S. P.; Hautier, G.; Chen, W.; Richards, W. D.; Dacek, S.; Cholia, S.; Gunter, D.; Skinner, D.; Ceder, G.; Persson, K. A. Commentary: The Materials Project: A Materials Genome Approach to Accelerating Materials Innovation. *APL Mater.*, **2013**, *1* (1), 011002. https://doi.org/10.1063/1.4812323.
- (37) Wang, L.; Maxisch, T.; Ceder, G. Oxidation Energies of Transition Metal Oxides within the GGA+U Framework. *Phys. Rev. B*, **2006**, *73* (19), 195107. https://doi.org/10.1103/PhysRevB.73.195107.
- (38) Blöchl, P. E. Projector Augmented-Wave Method. *Phys. Rev. B.*, **1994**, *50* (24), 17953–17979. https://doi.org/10.1103/PhysRevB.50.17953.
- (39) Monkhorst, H. J.; Pack, J. D. Special Points for Brillouin-Zone Integrations. *Phys. Rev. B*, **1976**, *13* (12), 5188–5192. https://doi.org/10.1103/PhysRevB.13.5188.
- (40) Makov, G.; Payne, M. C. Periodic Boundary Conditions in Ab Initio Calculations. *Phys. Rev. B*, **1995**, *51* (7), 4014–4022. https://doi.org/10.1103/PhysRevB.51.4014.
- (41) Henkelman, G.; Uberuaga, B. P.; Jónsson, H. A Climbing Image Nudged Elastic Band Method for Finding Saddle Points and Minimum Energy Paths. *J. Chem. Phys.*, **2000**, *113* (22), 9901–9904. https://doi.org/10.1063/1.1329672.
- (42) Heyden, A.; Bell, A. T.; Keil, F. J. Efficient Methods for Finding Transition States in Chemical Reactions: Comparison of Improved Dimer Method and Partitioned Rational Function Optimization Method. J. Chem. Phys., 2005, 123 (22), 224101. https://doi.org/10.1063/1.2104507.
- (43) Henkelman, G.; Jónsson, H. A Dimer Method for Finding Saddle Points on High Dimensional Potential Surfaces Using Only First Derivatives. *J. Chem. Phys.*, **1999**, *111* (15), 7010–7022. https://doi.org/10.1063/1.480097.
- (44) Olsen, R. A.; Kroes, G. J.; Henkelman, G.; Arnaldsson, A.; Jónsson, H. Comparison of Methods for Finding Saddle Points without Knowledge of the Final States. *J. Chem. Phys.*, 2004, 121 (20), 9776–9792. https://doi.org/10.1063/1.1809574.
- (45) Momma, K.; Izumi, F. VESTA 3 for Three-Dimensional Visualization of Crystal, Volumetric and Morphology Data. *J. Appl. Cryst.*, **2011**, *44* (6), 1272–1276. https://doi.org/10.1107/S0021889811038970.
- (46) Ammal, S. C.; Heyden, A. Modeling the Noble Metal/TiO₂ (110) Interface with Hybrid DFT Functionals: A Periodic Electrostatic Embedded Cluster Model Study. *J. Chem. Phys.*, **2010**, 133 (16), 164703. https://doi.org/10.1063/1.3497037.
- (47) Nørskov, J. K.; Rossmeisl, J.; Logadottir, A.; Lindqvist, L.; Kitchin, J. R.; Bligaard, T.; Jónsson, H. Origin of the Overpotential for Oxygen Reduction at a Fuel-Cell Cathode. *J. Phys. Chem. B*, 2004, 108 (46), 17886–17892. https://doi.org/10.1021/jp047349j.
- (48) Atkins, P. W.; Julio De Paula; Keeler, J. *Atkins' Physical Chemistry*; Oxford University Press: Oxford, 2018. pp 886

- (49) Peterson, A. A.; Abild-Pedersen, F.; Studt, F.; Rossmeisl, J.; Nørskov, J. K. How Copper Catalyzes the Electroreduction of Carbon Dioxide into Hydrocarbon Fuels. *Energy Environ. Sci.*, **2010**, *3* (9), 1311. https://doi.org/10.1039/c0ee00071j.
- (50) Yang, W.; Solomon, R. V.; Mamun, O.; Bond, J. Q.; Heyden, A. Investigation of the Reaction Mechanism of the Hydrodeoxygenation of Propionic Acid over a Rh(111) Surface: A First Principles Study. *J. Catal.*, **2020**, *391*, 98–110. https://doi.org/10.1016/j.jcat.2020.08.015.
- (51) Shampine, L. F.; Reichelt, M. W. The MATLAB Ode Suite. *SIAM J. Sci. Comput.*, **1997**, *18* (1), 1–22. https://doi.org/10.1137/S1064827594276424.
- (52) Stegelmann, C.; Andreasen, A.; Campbell, C. T. Degree of Rate Control: How Much the Energies of Intermediates and Transition States Control Rates. *J. Am. Chem. Soc.*, **2009**, 131 (23), 8077–8082. https://doi.org/10.1021/ja9000097.
- (53) Campbell, C. T. The Degree of Rate Control: A Powerful Tool for Catalysis Research. *ACS Catal.*, **2017**, *7* (4), 2770–2779. https://doi.org/10.1021/acscatal.7b00115.
- (54) Cheng, L.; Assary, R. S.; Qu, X.; Jain, A.; Ong, S. P.; Rajput, N. N.; Persson, K.; Curtiss, L. A. Accelerating Electrolyte Discovery for Energy Storage with High-Throughput Screening. *J. Phys. Chem. Lett.*, **2015**, *6* (2), 283–291. https://doi.org/10.1021/jz502319n.
- (55) Qu, X.; Jain, A.; Rajput, N. N.; Cheng, L.; Zhang, Y.; Ong, S. P.; Brafman, M.; Maginn, E.; Curtiss, L. A.; Persson, K. A. The Electrolyte Genome Project: A Big Data Approach in Battery Materials Discovery. *Comput. Mater. Sci.*, 2015, 103, 56–67. https://doi.org/10.1016/j.commatsci.2015.02.050.
- (56) Jung, M. H.; Alsmadi, A. M.; Chang, S.; Fitzsimmons, M. R.; Zhao, Y.; Lacerda, A. H.; Kawanaka, H.; El-Khatib, S.; Nakotte, H. Magnetic Ordering in Single-Crystalline SrLaFeO₄ and Sr_{1.1}La_{0.9}FeO₄. *J. Appl. Phys.*, **2005**, *97* (10), 10A926 https://doi.org/10.1063/1.1861416.
- (57) Sun, C.; Stimming, U. Recent Anode Advances in Solid Oxide Fuel Cells. *J. Power Sources*, **2007**, *171* (2), 247–260. https://doi.org/10.1016/j.jpowsour.2007.06.086.
- (58) Tealdi, C.; Ferrara, C.; Mustarelli, P.; Islam, M. S. Vacancy and Interstitial Oxide Ion Migration in Heavily Doped La_{2-x}Sr_xCoO_{4±δ}. J. Mater. Chem., 2012, 22 (18), 8969–8975. https://doi.org/10.1039/c2jm30769c.
- (59) Huan, D.; Wang, Z.; Wang, Z.; Peng, R.; Xia, C.; Lu, Y. High-Performanced Cathode with a Two-Layered R–P Structure for Intermediate Temperature Solid Oxide Fuel Cells. *ACS Appl. Mater. Interfaces*, **2016**, *8* (7), 4592–4599. https://doi.org/10.1021/acsami.5b10844.
- (60) Takamatsu, A.; Tamai, K.; Hosokawa, S.; Tanaka, T.; Ehara, M.; Fukuda, R. Oxidation and Storage Mechanisms for Nitrogen Oxides on Variously Terminated (001) Surfaces of SrFeO_{3-δ} and Sr₃Fe₂O_{7-δ} Perovskites. *ACS Appl Mater Interfaces* **2021**, *13* (6), 7216–7226. https://doi.org/10.1021/acsami.0c20724.

- (61) Gu, X. K.; Nikolla, E. Design of Ruddlesden-Popper Oxides with Optimal Surface Oxygen Exchange Properties for Oxygen Reduction and Evolution. *ACS Catal.*, **2017**, *7* (9), 5912–5920. https://doi.org/10.1021/acscatal.7b01483.
- (62) Kröger, F. A.; Vink, H. J. Relations between the Concentrations of Imperfections in Solids.
 J. Phys. Chem. Solids, 1958, 5 (3), 208–223. https://doi.org/10.1016/0022-3697(58)90069-6.
- (63) Bockris, J. O.; Nagy, Z. Symmetry Factor and Transfer Coefficient. A Source of Confusion in Electrode Kinetics. *J. Chem. Educ.*, **1973**, *50* (12), 839. https://doi.org/10.1021/ed050p839.
- (64) Xie, W.; Lee, Y. L.; Shao-Horn, Y.; Morgan, D. Oxygen Point Defect Chemistry in Ruddlesden–Popper Oxides $(La_{1-x}Sr_x)_2MO_{4\pm\delta}$ (M = Co, Ni, Cu). *J. Phys. Chem. Lett.*, **2016**, *7* (10), 1939–1944. https://doi.org/10.1021/acs.jpclett.6b00739.

For Table of Contents Only

